Title
A Lens into the Cu Nanograin by In Situ Vibrational Spectroscopy

Journal
Journal of the American Chemical Society, 148(21)

ISSN
0002-7863

Authors
Guzman, MariaV Fonseca
Shan, Yu
Wang, Tianle
et al.

Publication Date
2026-06-03

DOI
10.1021/jacs.5c22767

A Lens into the Cu Nanograin by *in situ* Vibrational Spectroscopy

Maria V. Fonseca Guzman[1,3,4,5], Yu Shan[2,3,4,5], Tianle Wang[1,3,5], Julian Feijoo[1,3,4], Nathan Liu[1], Jihoon Choi[2], Gabrielle Heuer[1], Andrew Liu[2], Peidong Yang[1,2,3,4,*]

[1]Department of Chemistry, University of California, Berkeley, CA 94720, USA

[2]Department of Materials Science and Engineering, University of California, Berkeley, CA 94720, USA.

[3]Chemical Sciences Division, Lawrence Berkeley National Laboratory, Berkeley, CA 94720, USA.

[4]Kavli Energy NanoScience Institute, Berkeley, CA 94720, USA.

[5]M.V.F.G., Y.S. and T.W. contributed equally; *Corresponding author: p_yang@berkeley.edu

Abstract

Cu-based catalysts are uniquely capable of C–C coupling during electrochemical CO_2 reduction (CO_2R), yet further mechanistic understanding remains hampered by the lack of spectroscopically resolved descriptors that demonstrate how surface adsorbates emerge and evolve within their catalytic environment. Here, we correlate *in situ* surface-enhanced Raman spectroscopy (SERS) and surface-enhanced infrared absorption spectroscopy (SEIRAS) to resolve the potential-dependent dynamics during CO_2R on Cu nanograin catalysts. By building on previous benchmarking of low overpotential performance and nanograin structural evolution, we offer a diagnostic framework linking vibrational signatures to catalytic function, unveiling which species appear, persist, and turnover as the electrified surface and interfacial environment evolve under bias. The onset of linear CO is marked below -0.45 V, coincident with persistent adsorbed *OH/*O domains beyond the CO_2R onset. In this context, Cu nanograins serve as a platform to dissect contributions of adsorbate coverage. By carefully dissecting the potential dependence of emergent twin-defect/step CO stretch bands (P1-P2), alongside the prototypical terrace-site CO stretch band (P3), we provide important context for interpreting coupled spectroscopic trends driven by coverage effects and resolve this for the evidently complex nanograin morphology. Together, these observations highlight the intertwined roles of surface stabilization and interfacial flux in steering multicarbon product formation. By directly linking vibrational signatures to catalytic behavior, this work aims to bridge the gap between observation and control and help guide towards a predictive framework of fine-tuned selectivity for CO_2R.

Introduction

Electrochemical reduction of carbon dioxide (CO_2R) on Cu remains a uniquely promising route toward the sustainable production of multi-carbon fuels and chemicals.[1,2] Among elemental catalysts, Cu alone sustains appreciable formation of products beyond CO, whereas Au, Ag, and many previously reported molecular catalysts terminate primarily at CO.[3–5] This distinctive behavior arises from Cu's ability to promote C–C coupling through a complex orchestration of *CO/*CO-derived intermediates.[6] Remarkably, this step takes place without direct electron transfer from the external circuit. Yet, the mechanistic origins of this capability remain poorly understood. Recent advances have enabled CO_2R on Cu to be scaled to industrially relevant current densities reaching hundreds of milliamperes for multicarbon products, thereby sharpening interest in how Cu functions under operating conditions and how its local reaction environment can more favorably direct product selectivity.[7,8] Single-pass selectivity windows across a broad range of operating potentials is also crucial for making high current density operation tractable. Linked to Cu's lower nobility ranking, this limitation is manifested in both the intrinsic dynamic speciation of Cu and the strong dependence of the 'pre-catalyst' or 'pristine' catalyst state in governing this evolution and resulting selectivity.[9,10] Although substantial progress has been made in detecting surface-bound intermediates, mechanistic understanding remains limited by an incomplete, often indirect, spectroscopic picture of the reactive intermediates and crucial bystander species under realistic conditions. Beyond detection alone, understanding how such species stabilize, interact, couple, and transform within their operative environments requires characterization methods with simultaneous surface sensitivity, spatial resolution, and cross-cutting time scales commensurate with catalytic turnover as well as 'slow' processes like catalyst reconstruction and aging; capabilities that are still only partially realized.[11,12]

Despite such sustained effort, the origins of selectivity on Cu remain incompletely understood, particularly in nanostructured forms of Cu, where low-coordinated active sites, interfacial electric fields, and local solvation effects differ significantly from those in planar analogues.[13–15] Complicating this picture is the phenomenon of reaction-driven evolution, wherein the catalyst surface itself dynamically restructures under operating conditions.[16,17] Nanograin architectures, for example, sustain extended reactive ensembles with long-range low coordination, rapid surface migration, and enhanced electric-field confinement; features associated with increased C_{2+} formation.[18] Yet, to some degree, even 'bulk' Cu surfaces can dynamically evolve to display some similar low-coordination domains under their operation.[19–21] Thus, real-time molecular-level insights into how these unique local environments evolve and proceed to govern the fate of intermediates remain essential. This work aims to marry the structural description of evolving Cu nanocatalysts under reactive environments with key spectral observables linked to CO_2R selectivity. By building convergent evidence using *in situ*, complementary vibrational probes, surface-enhanced Raman spectroscopy (SERS) (**Figure 1a**) and surface-enhanced infrared absorption spectroscopy (SEIRAS), we evaluate how spectral features arising at, adjacent to, or beyond active sites, surveyed across a broad potential range, inform conclusions about the intrinsic reactivity of Cu nanograins.

With this context in mind, we now turn to the physical origins of these effects at the atomic scale. As a starting point, lower coordination has long been recognized as a central driver of enhanced reactivity towards adsorbates. In contrast to bulk Cu, which should maintain a full d-orbital, nanograin aggregates, lingering transient Cu^+ species, and dangling bonds can lead to bands that maintain a higher proclivity for binding intermediates. More recently, it has been shown that polycrystalline domains coalescing into nanograin aggregates further amplify this behavior, suggesting that grain boundaries and their engineered interface represent a critical and previously underappreciated, active-site motif.[16,22–24]

Beyond the structure alone, catalyst performance trends increasingly point to the importance of the local reaction environment. Factors such as the management of local intermediate concentration and transport, altered dielectric environments, and restructuring of interfacial proton donors emerge as levers for steering selectivity.[25] For instance, hydrophobic environments help to concentrate CO_2 near active sites, overcoming its low solubility in water (~33 mM at 25 °C),[26,27] while molecular additives reshape hydrogen-bond networks to facilitate proton-coupled electron transfer.[28–30] Several studies have demonstrated that modulation of *CO binding and control of local intermediate concentration are central to overcoming selectivity barriers.[31,32] Viewed in this context, the similar activities observed across many nanograin-forming precursors are unsurprising. A notable exception is the *anomalously low activation C_{2+} overpotential of the 6.7 nm Cu nanograin catalyst* **(Figure 1b)**, which outperforms other Cu-derived, grain-like architectures by greater than ~30 mV.[24,33,34] Hypotheses include ligand-derived control over Cu's reduction rate,[35] as well as the hydrophobic surface led by the alkyl chains comprising ligand tails, which can partially give rise to concentrating CO_2 near active sites, as well as promoting high local *CO concentrations that extend residence times required to promote C–C coupling[36,37] and mitigate the HER onset, analogous to biological substrate channeling.

Consistent with this picture, previous isotopic-labeling experiments on ~7 nm Cu nanograins have revealed that local intermediate buildup influences C_2 onset potentials, with densities approaching intermediate crowding of ~100 molecules per surface atom and extended migration length scales observed.[32] These results imply that for mass-transport-limited reactions with competing pathways, local accumulation and surface mobility of intermediates may outweigh the binding strength of any single adsorbate in dictating selectivity. Similarly, activation events, especially for relatively hard to activate small molecules, appears to be the most thermodynamically limiting. Nevertheless, deliberately tuning surface diffusion and interfacial equilibration across the electrocatalytic interface under a constant charge flux and vast surface morphological changes remains extremely challenging. Yet these dynamic transport processes ultimately govern whether catalytic turnovers are activated or suppressed, underscoring their central role in defining steady-state performance.

Collectively, previous studies highlighting different contributions to the electrochemical behavior of the Cu nanograin demonstrate this system as an ideal platform for interrogating structure-activity relationships across multiple length scales and descriptors. This foundation enables us not only to rationalize performance trends, but also to identify mechanistic pathways by which Cu-based nanocatalysts may be further driven into low-overpotential regimes. Still, a

persistent gap remains between electrochemical descriptors and direct observation of surface intermediates under *operando* conditions. In this context, vibrational spectroscopy enters, offering a powerful lens into the mechanistic behavior of nanostructured Cu under biasing. First, SERS and SEIRAS differ fundamentally in their sensitivity to vibrational modes due to their respective selection rules. SERS preferentially enhances modes with large polarizability derivatives and is highly sensitive to local electromagnetic "hot spots," whereas SEIRAS is governed by the infrared surface selection rule and selectively enhances modes with dipole moments oriented normal to the interface. As a result, certain adsorption geometries and site populations may be preferentially detected by one technique over the other, yielding complementary views of the electrochemical interface and highlighting the value of combining both probes to better resolve evolving surface chemistry during CO_2 reduction.

Even so, assignment of species remains challenging due to overlapping bands, dynamic and evolving backgrounds and a complex population of surface-bound intermediates and spectators, with often similar vibrational fingerprints. This complexity calls for the implementation of robust experimental design and complimentary interpretive frameworks, using both techniques to gain *'complimentary'*, delivering something missing from the other technique, and '*correlative'* insights, helping to cross-validate across observational trends. Isotopic labeling strategies, especially substitution with $^{13}CO_2$ and D_2O, aid in distinguishing active intermediates from spurious contributions and spectators. These isotopic strategies serve as critical validation tools, anchoring spectral interpretation in chemical specificity and mechanistic relevance. Careful implementation of *in situ* measurements, with awareness of catalyst evolution, mass transport, buffering, and convection during spectroscopic measurements, is essential for replicating electrochemical CO_2R environments and interpreting which motifs truly contribute to our emerging mechanistic picture.[31,38]

Methods

in situ Electrochemical Raman Spectroscopy

By contrast with *ex situ* methods, *in situ* electrochemical Raman spectroscopy provides a powerful means of tracking reaction intermediates at electrified interfaces under operating conditions. The interpretation of Raman intensities in these environments must contend with unequal cross sections, intensity fluctuations, and selective SERS enhancement of specific vibrational modes, hallmarks of surface-enhanced Raman scattering (SERS), which complicate direct comparisons of adsorbate coverages and local concentrations.[39–42] In particular, nanoparticle-based plasmonic substrates not only amplify Raman absorption and scattering but do so in a strongly geometry- and frequency-dependent manner, selectively enhancing vibrational modes that couple efficiently to (or are 'resonant' with) localized electromagnetic fields. Record detection of single molecule analytes achieved under optimized SERS has been demonstrated down to sub-nanomolar concentrations (~ 10^{-10} M). Such demonstrations typically employ high–Raman-cross-section dyes as the probe molecule, for which effective SERS cross sections are as large as ~10^{-16} cm^2 $molecule^{-1}$. In comparison, the absolute differential Raman scattering cross sections of small diatomic molecules in the visible are much smaller (~10^{-31}–10^{-30} cm^2 sr^{-1} $molecule^{-1}$; e.g., N_2 at 514.5 nm is ~4 × 10^{-31} cm^2 sr^{-1}), placing them in a far less

favorable observability regime. In effect, SERS signals can also be 'site-biased', as higher observability of high field sites can dominate the spectrogram. Yet, the decaying field strength from resonant surfaces remains highly useful and maintains prominent surface sensitivity relevant to catalysis.

Many existing reports of *in situ* Raman experiments that probe CO_2R rely on roughened Cu foils. These Cu surfaces can be pre-activated by electrochemical cycling to enhance SERS while deviating the surface morphology. However, we could not rely on such pre-activation due to the fragility of the nanograin architecture and our strict goal of reproducing previously reported performance conditions with the highest possible fidelity. Accordingly, SERS architectures were employed to lend crucial signal enhancement near Cu. Au nanocubes supported on Au films were deliberately used as SERS amplifiers (**Figure 1c, Figure S1**), leveraging their well-defined geometry and strong near-field enhancement while the underlying Au film served as an optically reflective mirror to maximize scattering collection efficiency. SERS measurements were mostly conducted with 633 nm to allow assessing the full spectral window out to 4,000 cm^{-1} (**Figure S2**).

Significantly, mass transport further governs the operando Raman spectral response during CO_2R. Au substrates, for instance, not only serve as plasmonic amplifiers but likewise function as local CO generators that potentially downshift the onset potentials for C_{2+} products, which can enhance the observability of downstream intermediates.[1,43,44] Reproducing optimal CO_2R conditions across *in situ/operando* techniques still remains an open investigation across the field. For *in situ* SERS, the main concern is local mass transport. The confocal configuration prevents stirring of the electrolyte solution. Under stagnant electrolyte conditions, artificially thick boundary layers promote local accumulation of CO and exaggerate CO stretch intensities. This remains consistent since high boundary-layer thicknesses reduce interfacial field confinement and correlate with diminished reactivity. Accordingly, flow-cell architectures mitigate this effect by imposing forced convection, thereby producing a steady CO_2 flux by reducing the boundary-layer thickness.[31] This boosts the local concentration of CO_2 and yields conditions that more faithfully replicate catalytic operating regimes (**SI Discussion I**). The positive reaction order with respect to CO_2 implies that thinner boundary layers, by boosting local convection with flow of electrolyte to enhance interfacial CO_2 flux, directly increases the catalytic current density. However, due to sporadic bubble formation, it remains challenging to reliably replicate quantitative boundary-layer thicknesses. As such, interpretations must be contextualized and grapple with the realistic dynamics of the electrochemical interface. Ultimately, these factors, ranging from enhancement physics to cell architecture, determine the temporal resolution and mechanistic fidelity attainable for *in situ* SERS studies of CO_2 electroreduction.

Results and Discussion

Potential-Dependent Surface Speciation and Early CO Binding Modes

Characterization of pristine 6.7 nm Cu particles, at open circuit voltage (OCV) on SERS substrates, revealed vibrational signatures consistent with Cu_2O (T_2g mode at ~532 cm^{-1}) and CuO_x (~628 cm^{-1}).[45] The spectrum, labeled '*Initial*', does not represent an electrochemically equilibrated interface, as surface ligand coverage and a partially oxidized Cu surface limit electrolyte wetting and suppress carbonate coordination prior to the application of cathodic bias (**Figure 2a**).[13] Upon cathodic polarization, these oxide-related bands progressively diminish and eventually disappear by ~-0.20 V vs RHE, indicating electrochemical reduction of bulk oxides. While electrochemical reduction establishes the metallic Cu surface required for catalysis, the emergence of CO_2 reduction activity is not dictated by surface composition alone. Rather, upon the onset of metallic Cu exposure, the local chemical environment at the interface becomes the dominant factor governing reaction onset, intermediate stability, and selectivity under applied bias.

Spectroscopic analysis prior to the onset of CO_2 electroreduction reveals distinct vibrational features that signal transformations in the Cu surface layer composition, in part originating from the 0.1 M $KHCO_3$ electrolyte. Modes from carbonate/bicarbonate species are expected at very moderate biasing potentials, as carbonate adsorption is driven by interfacial charge compensation and coordination to residual surface Cu–*O/*OH, classic non-faradaic adsorption, rather than by the kinetically demanding activation of CO_2, which requires electron-transfer and bond activation/rearrangement. Between -0.10 and -0.30 V vs RHE, characteristic peaks emerge near 315-360, 712 cm^{-1}, 1070 cm^{-1}, and 1525 cm^{-1} (**Figure 2a, Figure S3**). Two peaks are resolved below 400 cm^{-1}, a band near 315 cm^{-1}, and a second band around 360 cm^{-1}. Tracking the potential dependent behavior, only one of these components, 360 cm^{-1}, correlates consistently with the 1525 cm^{-1} feature (**Figure S4b**), supporting its assignment to the same surface-bound bidentate $*O_2CO$ species.[46–50] Furthermore, neither 360 nor 1525 cm^{-1} peaks are shifted under D_2O exchange (**Figure S5**).

The independent potential dependence of the ~1070 cm^{-1} band indicates that it originates from interfacial (free or weakly associated) carbonate species, distinct from the specifically adsorbed bidentate carbonate signatures captured by ~360 and ~1525 cm^{-1}. Minimal Stark response of the ~1070 cm^{-1} symmetric stretch is expected due to its weaker sensitivity to changes in the surface electric field, consistent with interfacial CO_3^{2-} (**Figure S4e**). In contrast, discernable Stark shifts occur in the ~360 and ~1525 cm^{-1} band reflect stronger surface coupling and electric field sensitivity, indicative of surface-bound species (**Figure S4f-g**). However, we cannot dismiss that the evolving surface structure may also be operative in the fluctuations of peak locations, instead of pure Stark interpretation.

Interfacial transport and reaction kinetics, rather than bulk equilibrium, dominate selectivity outcomes in CO_2 electroreduction. CO_2 availability at the interface is governed not only by diffusive transport but also by dynamic bicarbonate-carbonate equilibria that facilitates the local supply/replenishment of CO_2 availability through interconversion kinetics.[51] Thus, we should expect both CO_3^{2-} and HCO_3^- to appear in SERS measurements. Both species should exhibit in-plane and out-of-plane bending/deformation modes. While generally thought to be weaker modes, their activity can be boosted near surfaces. A peak at 706-715 cm^{-1} appears throughout a wide potential range, and its inflection appears correlated with bicarbonate/carbonate surface equilibrium (**Figure S4d**). This mode does not shift

under D_2O exchange, supporting the assignment of in-plane bending mode for free $\delta(CO_3^{2-}/HCO_3^-)$ and monodentate $\delta(OCO_2^-)$ carbonate, as opposed to the *OH libration/deformation δ(*O-H) where O-D would be appreciably shifted (**Table S1**). Note that even HCO_3^- modes can be H/D exchange invariant since the vibration is mainly in the $\{CO_3\}$ skeleton and not involving the O-H coordinate. Weaker spectral features at ~853 and ~1314 cm^{-1} over this potential range are consistent with the out-of-plane bending/deformation $\gamma(CO_3^{2-})$/ $\gamma(OCO_2^-)$ and symmetric stretching modes of bidentate and monodentate carbonate (CO_3^{2-}), respectively (**Figures S6–S7, Table S2**), evolving within the same potential window.

The remaining low-frequency component near 315 cm^{-1} eventually, near -0.43 V, blends into a mode which is confidently ascribed for atop-CO frustrated rotation (Cu-*CO_{LR}). It may plausibly reflect Cu-*C liberation or hindered rotational motion, or Cu-O/$Cu(OH)_x$ deformations involved during the evolution of surface Cu.[46,52] However, this is only speculative at this time. We observe modes appear during the transformation of surface Cu^+ to fully metallic Cu^0.[53] Accordingly, we interpret carbonate-related features not as discrete competitive adsorption but rather as disordered carbonate adlayers stabilized during surface/bulk phase reconstruction. This view is consistent with *in situ* STM and SXRD observations made by Cuenya, Kley and co-workers, that carbonate replacement by carboxy- species, and subsequent replacement by CO, correlate with structural transitions of the Cu surface.[13,54,55,56]

Furthermore, within the pre-CO_2R regime, marked by the absence of Cu–*CO low-frequency modes (280–360 cm^{-1}), sharp CO stretches at ~1980 cm^{-1} were transiently observed, indicating bridged *CO species under the initial stages of biasing at ~-0.16 V vs RHE (**Figure 3**). These features are transient, and then spectra are dominated by atop-bound CO modes, confirming the transient nature of bridged *CO coordination under continuous polarization. Experimentally, the ~1980 cm^{-1} feature appears predominantly during the initial reduction and activation of the catalyst and diminishes as the surface evolves under reaction conditions. We therefore interpret this instability as reflecting the evolving surface structure and site distribution, rather than intrinsic thermodynamic instability of the adsorbate itself. This 'stochastic CO' regime, as termed in previous reports, has been shown to be sensitive to plasmonic effects, particularly under 633 nm excitation that resonates with Cu nanostructures.[50,57] However, the lack of consistent corroborating low-frequency modes for atop/linear-CO suggests that these features do not directly modulate activation barriers in a way that drives harnessable, or even observable, CO_2R enhancements. Instead, they may reflect CO's well-established role as a restructuring agent: a species which can bind strongly enough to 'harpoon' atoms of Cu or direct surface-limited migration, inducing local reorganization or even ejection of Cu atoms.[16] This suggests involvement in surface restructuring processes prior to stable CO adsorption. Mainly, early emergence of carbonate and hydroxide adlayers perturbs Cu–Cu bonding, locally modulates surface charge, and compete directly with CO. This supports an interface that is structurally and electronically dynamic on the timescale of CO adsorption, from which spurious CO modes originate. These stochastic modes are reproduced under isotopic-substitution electrolysis in 0.1 $KDCO_3$ (**Figure S8**). The broad envelope of CO stretches between 2000–2100 cm^{-1}, however, makes it nearly impossible to infer site specificity. Moreover, the observed differences arise from time-dependent evolution of the catalyst surface, including changes in local structure, adsorbate populations, SERS, etc. that occur even under constant potential (**Figure 3d, Figure S9**).

Only after monodentate and free carbonate species dominate can we observe a clearer balance between CO and CO_3^{2-} adsorption at the surface (**Figure 2b**). Several studies have examined competitive adsorption between carbonate species and CO-derived intermediates on Cu electrodes under related conditions. The discussion here instead emphasizes the observed spectroscopic evolution without invoking a specific competitive adsorption framework, which would usually imply that low overpotential CO_2R activity is limited *solely* by site availability. The absence of a strong *CO signal at potentials where carbonate is already partially removed may reflect insufficient driving force for CO_2/CO activation or low steady-state coverage of CO at those biases, rather than genuine blocking or competitive adsorption by residual carbonate.

With increasing bias, the onset of 'atop'/'linear' CO binding is observed, suggesting that complete reduction, restructuring steps, removal of blocking species, and energetic driving force must occur before preferential 'atop'/'linear' *CO adsorption can dominate. At this stage, at least three *CO-related bands, mainly νCu-*CO_{LR} = 'linear Cu-CO frustrated rotation' at 285-308 cm^{-1}, νCu-*$C(O)_{LS}$ = 'linear Cu-C(O) stretch' at 380-390 cm^{-1} (**Figure 2b, Figure S10-13, Table S3**) and ν_sCO = 'C-O stretch' at ~2040-2140 cm^{-1} (**Figure 3**) are expected. Isotopic labeling experiments further support the assignments of the low-frequency Cu–CO modes, as distinct ^{13}C sensitivities were observed for the frustrated rotational and Cu-C(O) coordinates. The νCu-*CO_{LR} feature exhibits a modest shift of +2.55 to +3.35 cm^{-1}, consistent with limited carbon involvement in the rotational coordinate, whereas the νCu-*$C(O)_{LS}$ mode shows a larger shift of −9.05 to −10.80 cm^{-1}, reflecting greater participation of Carbon motion in the vibrational mode and reinforcing that these bands arise from distinct metal-adsorbate vibrations (**Figure 4, Figure S14, Table S8**).

These two modes corresponding to 'atop'/'linear' CO appear alongside additional modes near 1385, 1445 and 1600 cm^{-1} (**Figures S4c, S6-S7, S13, Table S2).** Modes at 1380-1390 cm^{-1} and 1556-1610 cm^{-1} are assigned to symmetric and asymmetric carboxylate (*CO_2^-) vibrations, respectively. By comparison, the asymmetric carboxylate mode is far more Raman-active (typically 4-5× stronger than the symmetric mode), which plausibly explains why it's observed more strongly and consistently. None of the 1390, 1445 and 1600 cm^{-1} features shift with D_2O exchange (**Figure S5**). This can support the remaining assignment of 1445 cm^{-1} to the $\nu_{as}(CO_3^{2-})$. Assignments for CO_3^{2-}, HCO_3^- and *CO_2^- asymmetric stretching modes are indicated at 1445 and 1600 cm^{-1}, respectively (**Figure 2b**). Contributions from a CO dimer–derived intermediate ($OCCO^-$) have also been reported in the ~1445 cm^{-1} region. Given the known spectral overlap in this region, these assignments are considered within the context of isotope shifts (**Figure S5**), as well as correlation and potential dependence across their spectral evolution (**Figure S4**). The 1445 cm^{-1} peak appears as early as -0.18 V, hence it has a minimal correlation with high CO coverage, as expected for an OCCO- mode. The spectral feature near ~900 cm^{-1}, which emerges around -0.48 V, is consistent with deformation $\delta(HCO_3^-)$ mode, which couples O-C-O + O-H motion (**Figure 2b**). It should also be noted that local pH changes as a function of applied potential may shift the position of carbonate modes, hence the range of tens of wavenumber reported (**Table S1**).[46,50,58–62] Protonation/deprotonation of surface-adsorbed carbonate, bicarbonate, or carboxylate would be expected to tune vibrational frequencies; binding modality can further split modes. Meanwhile, the precise binding state (weakly bound vs free electrolyte species) remains in part potential-dependent and in part stochastic under electrocatalytic conditions.

Given the ubiquity of carbonate adlayer formation and its potential role in gating over a significant low overpotential region of potential catalytic conversion, we investigated whether this phenomenon represents a critical step in the reconstruction process under CO_2R conditions. Compared with CO_2, electrolyte anions are initially more strongly stabilized at the Cu surface, consistent with their facile activation during early polarization. This observation raises the broader question of whether controlling buffering kinetics and thereby modulating the residence time and displacement behavior of adsorbed carbonate, may provide an additional handle for steering selectivity. Notably, prior studies have reported that strong modes from carbonate surface adsorption emerge only when evolving from the Cu_2O phase, but not from CuO phases, a distinction that remains unexplained but underscores the structural sensitivity of carbonate attachment.[54] This reactivity also emphasizes how complex carbonate chemistry can be hosted on Cu/Cu^+, in comparison with more noble metals, observed tangibly within the abundant Cu-based minerals formed within nature. Thus, we anticipate that this surface chemistry contributes to complicating potential reconstruction pathways and even gating, though not solely from this assessment, the ability to access lower overpotential CO_2 conversion. This underscores the central role of surface chemistry in governing reconstruction and reactivity on Cu.

Transition to Active CO Binding and Onset of CO_2R

In nanostructured Cu systems, *CO accumulation persists to a greater extent than on planar analogues, consistent with the high density of undercoordinated sites, enlarged electrochemically active surface area, and distinct migration length scales characteristic of nanograin architectures.[16] The selectivity and kinetics of CO_2R pathways are strongly influenced by local surface faceting, binding site coordination, reactant availability, and *CO coverage. At intermediate potentials, clear spectral signatures of 'atop'/'linear'-bound CO emerge (**Figure 2b**). The low-frequency vibrational region exhibits systematic evolution of features associated with Cu–*CO_{LR} frustrated rotation mode (νCu-*CO_{LR}) (**Figure 2b**) and Cu–$C(O)_{LS}$ stretching mode (νCu-*CO_{LS}) across biasing potential (**Figure 3**).[63] A comprehensive summary of peak fitting results is provided in **Tables S2-S8**, with representative datasets shown in **Figures S10-S14**. Notably, experiments performed on Cu nanocatalysts supported on bare glassy carbon electrodes, no underlying SERS substrate (**Figure S15-S16, Table S7**), reproduce similar trends. This helps support the assignment of these modes to Cu–CO interactions rather than to substrate effects. Under potentiostatic conditions, the ratio of 'atop'/'linear' CO frustrated rotation to stretch evolved consistently with surface coverage, reflecting hindered Cu–CO frustrated rotation at high *CO densities, in agreement with previous reports, attributing changes in this ratio to steric crowding and lateral interactions among adsorbed CO, and by implication, any other co-adsorbates as well.[59,64] To echo these reports, we find that the CO_{LS}/CO_{LR} equilibrates to a higher ratio with increased negative biasing, marking the transition into a higher surface coverage regime associated with active CO_2 reduction.

Notably, strong CO peaks persist as a complex band arises near -0.48 V to -0.98 V vs RHE, centered around 525 cm^{-1}, which represents mainly atop hydroxide co-adsorbates (**Figure 2a**, **Figure S10**). The behavior within this region will be elaborated in the following section. This is consistent with continuous renewal of CO intermediates under catalytic operation and that severe mass transport limitations are not being encountered under experimental conditions (**Figure S10-13**). Otherwise, transport would wipe away *CO signatures with increasing current density. Alternatively, what could happen is if the rate of CO_2 regeneration from HCO_3^- cannot match interfacial consumption, CO_2 may become locally depleted, and the reaction shifts toward competitive hydrogen evolution reaction (HER). While pK_a values define the thermodynamic buffering regime, the kinetics of these equilibria ultimately determine whether CO_2 reduction remains viable at the interface or yields HER and would significantly disrupt probing at appreciable CO coverage regimes relevant for downstream CO_2R. In tandem, no evidence for an atop-to-bridged CO transition was observed for ν(CO) once the 'linear'/'atop' CO onset was reached and stabilized, confirming that atop CO serves as the reactive intermediate, underscoring the critical importance of faithfully reproducing the nanograin architecture to sustain catalytic activity.[65]

Detection of Hydroxide and Surface Oxygen Co-Adsorbates

To further rationalize the low-overpotential behavior of Cu nanocatalysts, it is essential to resolve the identity, stability, and function of surface co-adsorbates, as these species strongly modulate apparent overpotentials and catalytic selectivity. Raman spectra reveal a complex band around 525 cm^{-1} consistent with surface-bound hydroxyl (*OH) species (**Figure 2b**). Reported geometries for *OH binding on Cu surfaces span atop, bridge, and hollow configurations, with corresponding Cu–*OH vibrational shifts reported near ~525, ~490 cm^{-1} and ~630 cm^{-1}, respectively. Similarly to *CO binding coordination, the ratios of bridged versus atop *OH can arise from amorphous versus grain-rich morphologies.[64] Isotopic substitution supports these assignments: the complex band near ~525 cm^{-1} exhibits measurable shifts upon isotopic exchange with D_2O (**Figure 4**), indicating contributions from multiple hydrogen-containing species bound to Cu.[63] The low grating number (600) employed for Raman experiments currently limits spectral resolutions which could aid improved isotopic deconvolution. However, improved resolution would come at a significant cost of spectral range an intensity. In contrast, the mode near 603 cm^{-1} remained invariant under both $^{13}CO_2$ and D_2O exchange and was therefore assigned to lattice-bound *O.[45,66,67] These features persist even in the absence of Au nanocubes (**Figure S15-16**), confirming their intrinsic association with the Cu surface. With increasing cathodic biasing, suppression and broadening of the $\nu_s(CO_3^{2-})$ signal could mark the displacement by reaction intermediates, repulsion by increased cathodic polarization, equilibrium shift towards bicarbonate generation, and interactions with oxy-species that emerge above the CO_2R onset (**Figure 2b**).

Beyond their spectroscopic signatures, 'oxy-'species, *OH and *O, exert functional control over interfacial reactivity through modifying the electronic boundary conditions at Cu surface atoms. Oxy- species are non-innocent, capable of transient charge storage and redistribution that shapes the local electronic structure of Cu active sites. In this sense, *O/*OH behaves as coupled proton-electron reservoirs, dynamically modulating electron density and stabilizing charged intermediates during turnover.[8,68–70] Concurrently, *O and *OH perturb the hydrogen-bonding network within the compact (Stern) layer by reorienting interfacial water and local ion structures, thereby modifying proton activity, field screening, and hydrogen-bond-mediated stabilization of adsorbates. Explicitly, they can promote lateral adsorbate interactions, including as leaving group anchors. Partially oxidized $Cu^{\delta+}$ formed in the presence of oxy-species may strengthen CO_2 binding through Lewis acidity, though the role of site competition has not been specifically analyzed.[71–73] Reported calculations suggest that oxy-species can stabilize key intermediate, underscoring their direct participation in the reaction landscape rather than a spectator role.[67]

Electrostatically, co-adsorbates introduce a second level of control. Terminal oxo groups (*=O) are intrinsically dipolar, with reported dipole moments on the order of 3–5 D.[74] Strongly dipolar species impose pronounced interfacial electric fields that shift surface work functions, reshape local potential profiles, and thereby modify charge-transfer barriers. The same dipolar character also accounts for the strong vibrational intensities of oxo-containing species observed spectroscopically, as their oscillatory motions couple efficiently to the local electromagnetic field. Collectively, these electrostatic contributions modify adsorption energies, influence neighboring bond polarization, and bias reaction pathways via field-driven stabilization of charged transition states.[75]

Structurally, *O and *OH may also stabilize low-coordination Cu atoms and transient adatom clusters formed during cathodic reconstruction.[10] By competing with CO-driven surface migration, oxy-species may transiently pin under-coordinated atoms and raise diffusion barriers to surface migration,[76,77] thereby slowing coarsening. Nanograins, which host a large density of defects, boundaries, and undercoordinated sites, support the formation of oxy-species. Under sufficiently high local pH attainable after triggering appreciable CO_2R current densities, driven by OH^- accumulation during CO_2 reduction, these oxy-species might remain present well beyond expectations for bulk-phase thermodynamics.[45,78,79] Overall, species coverage is well informed from SERS experiments, especially the joint presence of *OH/*O and *CO. This must be implemented in evaluating plausible mechanistic pictures. Not only is OH^- formed stoichiometrically at the interface as a byproduct of CO_2 reduction, but *OH/*O become bound to the Cu surface. Thus, oxy- species are implicated to influence local adsorption electronics of *CO and other reactive intermediates, influencing the reaction landscape through electrostatics, disruption of dipole-dipole CO-CO interactions, and impacting reconstruction and diffusional barriers. In tandem, *O can potentially serve as a 'defective' surface adsorption site, impacting chemical outcomes.[80–82]

Rather than being passive spectators, co-adsorbates operate as active modifiers of the surface's electronic and structural boundary conditions. These effects therefore reshape not only surface reactivity but also the spectroscopic response itself, as charge redistribution and dipole coupling amongst neighboring adsorbates modifies vibrational intensities, selection rules, and field-dependent line shapes observed under *operando c*onditions. Together, these observations support a kinetic gating model in which carbonate adlayers and hydroxide regulate reconstruction, active-site exposure, and intermediate stability, before and after the onset of linear CO, respectively, through their competitive adsorption and displacement dynamics. These findings further suggest that, on Cu, deliberate control over interfacial electrostatics may be tightly interwoven with morphological evolution and is equally important to consider in targeting low-overpotential performance.

SEIRAS as a Complementary Survey

To extend the mechanistic picture obtained from *operando* Raman measurements on Cu nanograins, surface-enhanced infrared absorption spectroscopy (SEIRAS) is employed as a complementary probe.[83,84] While Raman excels at metal–adsorbate and lattice modes, SEIRAS selectively amplifies dipoles aligned normal to the metal surface and therefore excels at probing C–O, C–H, and other polar stretching modes.[85,86] In addition, SEIRAS offers superior temporal resolution, enabling direct tracking of the sub-second/second(s) response of surface intermediates to electrochemical perturbations.[87] **Figure 4a** summarizes the overall SEIRAS workflow. Monolayer Cu nanograin films were loaded onto an SEIRAS-active Au films. To monitor the evolving interfacial environment of Cu nanograins, SEIRAS spectra were acquired during a series of synchronized linear-sweep voltammetry (LSV) scans, each referenced to a spectrum acquired at its respective starting potential (**Figure 5a**).

Nanoparticles loaded onto the SEIRAS substrate undergo electrochemical pre-conditioning during LSV 1, which sweeps from open-circuit voltage (≈ 0.6 V) to – 1.0 V vs RHE. The first notable spectral signatures are negative-going ν(C-H) features between 2800-2900 cm^{-1}, assigned to the alkyl chains of TDPA ligands (**Figure S17-18**), which indicate ligand removal under cathodic bias. Although transient, surface ligand desorption likely conditions nanograin aggregation.[24,88] As shown in **Figure 5b**, around –0.5 V, where adsorbed 'atop'/'linear' *CO is typically observed on Cu surfaces[89–91], a negative-going ("anti-absorption") feature is detected at ~2080 cm^{-1}, near the C–O stretch of linearly bound CO. Because the reference spectrum was collected at OCV, where CO adsorption is impossible, the observed negative band cannot be interpreted as a loss of adsorbed CO. While Fano interference often shows as derivative-like peak, we do not assign the P1 feature to a Fano mechanism, which is only applicable to describe coupling between a discrete vibrational mode and an underlying electronic or optical continuum. Instead, we use the derivative lineshape, which can be produced from several proofs including pure optical effects (effective medium theory, EMT), as a convenient phenomenological description of the observed asymmetry (**SI Discussion II**). [92–96] EMT predicts that geometric factors intrinsic to nanostructured systems, such as nanoparticle aggregation, film thickness, and interparticle spacing, can substantially modulate the effective interfacial dielectric constant, thereby dictating the intensity and asymmetry of infrared absorption features.[92,96] In the present system, dynamic aggregation of Cu nanograins similarly alters the local dielectric environment and creates geometric configurations that influence the interfacial optical response. Thus, the dip in LSV 1 is likely related to this evolving background. Fitting the line shape with a derivative like lineshape successfully reproduces the observed inversion near ~2100 cm^{-1} (**Figure S19**), but a mechanistically agnostic fitting is quite applicable here.

LSV 2 is performed immediately after LSV 1, with the scan window adjusted to 0 to -1.0 V to avoid reoxidation of Cu. The purpose of LSV 2 is to ensure complete ligand removal and nanograin aggregation so that the SEIRAS spectra collected in subsequent scans reflect a relatively stabilized interfacial environment and probe exclusively the steady-state behavior of the Cu nanograins. The SEIRAS spectra obtained during LSV 3, which also sweeps from 0 to –1.0 V, are discussed in greater detail below. As the potential becomes more cathodic, a negative band centered near 1480

cm^{-1} gradually develops (**Figure S20a**), corresponding to the desorption of bidentate carbonate, which is consistently reported.[89,97] Notably, the carbonate dynamics captured by SEIRAS closely mirror those revealed in SERS experiments (**Figure S4**): the intensity of the bidentate carbonate features plateaus near –0.4 V (**Figure S20b**), consistent with complete detachment and close to the emergence of atop-bound CO bands between 2000 and 2100 cm^{-1} (**Figure 2b, Figure 5b**).[98] From comparison to CO stretch locations observed in SERS (**Figure S9**), SEIRAS appears to agree well. At increasingly negative potentials, CO adsorption features steadily increase in intensity, accompanied by potential-dependent trends in C–H vibrational modes (**Figure S18**). Because the ligands have been entirely removed, the observed C–H modes most likely arise from a buildup of C–H–containing reaction intermediates (e.g., *Cu–C(R) and Cu-C(H)R, where R is any possible structural motif which follows the CO_2R pathway). Given the wide range of possible intermediates that exhibit C–H vibrations, however, assignment of this band to a specific species is not feasible.

Notably, CO adsorption on the Cu nanograins evolves into a multi-component C-O stretch lineshape at more negative potentials. Deconvolution of the atop-CO region requires three distinct spectral contributions (P1–P3): P1 at ~2083 cm^{-1}, P2 at ~2070 cm^{-1}, and P3 at ~2050 cm^{-1} (**Figure 5c**). Two of these bands correspond to well-established binding configurations on Cu surfaces.[92–94,99–102] P2 is related to step/edge-site adsorption, and P3 originates from terrace-site adsorption, both of which are commonly reported across common Cu catalysts and reproduced for Cu films.[90,91,103–108]

Regarding the high-frequency P1 component, although one might be tempted to attribute this band to a new and distinctive CO adsorption site, one must consider the impacts of coverage of strong dipole adsorbates in fundamentally skewing the selection rule of SEIRAS. To further interrogate the CO adsorption sites associated with P1-P3, SEIRAS spectra were collected during cathodic sweep (LSV 3), followed by an anodic sweep (LSV 4) and a subsequent cathodic sweep (LSV 5). **Figure 5d** summarizes the bias-dependent evolution of the CO stretching modes under alternating LSV scans. Firstly, the reversibility of the twin P1/P2 pattern in cyclic sweeps indicates that their appearance is governed by *electrostatics and screening*, rather than by irreversible restructuring of the Cu surface. Consistent with this interpretation, extended chronoamperometric measurements conducted at –0.84 V following LSV 5 (**Figure S24d**) confirm that P1-P3 bands persist under steady-state CO_2R operating conditions.

The frequency shifts and integrated areas as a function of potential of the P1–P3 components extracted from LSVs 3-5 and the subsequent chronoamperometry are summarized in **Figures S30–S31**. Notably, once the potential is driven more cathodically than –0.60 V, at which point the P1 feature becomes prominent, P1 and P2 exhibit strikingly similar behavior across all scans, displaying nearly identical bias-induced frequency shifts and comparable tuning rates (**Figure S29**). This strong correlation suggests that both components originate from CO molecules adsorbed at defect-rich sites, such as steps, edges, kinks, or grain boundaries, which share similar intrinsic vibrational frequencies. Importantly, although they arise from similar adsorption environments, P1 and P2 retain distinct vibrational frequencies and line shapes, consistent with subtle differences in local coordination or interfacial conditions.

Rather than definitive redistribution of active sites, the combined evolution of P1, P2, and P3 peak positions and integrated areas is interpreted in terms of Stark tuning and field-dependent reorientation, together with coverage (dipole-dipole) effects involving CO and co-adsorbate adsorption regimes. Tuning was independently analyzed for P1, P2, and P3 (**Figure S28**). To further assess the extent to which dipole-dipole coupling contributes to the P1 lineshape, the peak areas of P1–P3 extracted from LSVs 3–5 are summarized in **Figure S26**. Peak fittings reveal an isotherm-like ('s-shaped') trace for integrated peak area versus potential. These traces reveal distinctive responses, or hysteresis, between cathodic and anodic scan directions (**Figure S31**). If strong dipole-dipole coupling was the dominant factor, one would expect pronounced 'intensity borrowing', specifically, enhancement of the highest-frequency mode (P1) accompanied by depletion of the lowest-frequency mode (P3). The absence of such intensity redistribution cannot be thoroughly elaborated at this time. We attribute the limited strength of dipole–dipole coupling on Cu nanograins to the presence of substantial co-adsorbates, such as *O and *OH species, between neighboring *CO molecules. These co-adsorbates, independently probed by SERS, disrupt coherent dipole coupling and suppress a major manifestation of a shift in the selection rule.

Because the infrared intensity of *CO adsorbed at defect sites can be significantly amplified through dipole-dipole coupling, we next examined the intensity of the P1 feature under conditions which we expect to vary surface coverage.[103,109] As intermolecular dipole-dipole coupling scales with CO coverage, its contribution can be systematically modulated through online gas-switching experiments.[110,111] Upon switching the feed gas from CO_2 to N_2, almost immediately both P1 and P2 undergo a synchronized red shift (**Figures S33-34**), indicating that P1, like P2, is also sensitive to dipole–dipole interactions among adsorbed *CO molecules.

SEIRAS experiments performed on electroless deposited Cu films in 0.1 M $KHCO_3$ and 0.1 M $CsHCO_3$ (**Figure S21–S23**, **S35**) reproduce the characteristic evolution of *CO bands, while revealing systematic changes in the relative prominence of the P1 feature that reflect a dependence on emergent nanostructuring and electrolyte cation effects.[84,108,112–114] Owing to its larger ionic radius, Cs^+ is known to produce stronger interfacial electric fields, which can help promote CO_2 adsorption, stabilize *CO and $OCCO^-$ intermediates.[115,116] This will usually lead to enhancements in CO coverage, and a strong promotion of C-C coupling.[117,118] Under Cs^+, bridged CO is observed along with atop CO, unlike in the Cu nanograins where only atop CO was captured. In the context of principal evidence of P1-P3 co-existence on Cu nanograins (in the case of 0.1 M $KHCO_3$), the observed enhancement of P1 in 0.1 M $CsHCO_3$ electrolyte on Cu film is therefore taken as consistent with a broader sensitivity of this feature to interfacial conditions, without implying a direct causal role of the cation. Importantly, this interpretation obviates the need to invoke a distinctive CO adsorption site unique to Cu nanograins. These observations mainly indicate that behavior of the P1–P3 CO stretches arise from interplay of coverage, field effects, and in relation to Cu interfacial chemistry (**SI Discussion III**). This is not to dismiss the importance or possibility of 'dual-site' or 'tandem' architectures is well established in heterogeneous catalysis, including in proposed dual site Cu^0-Cu^+ mechanisms,[119–121] supported Pt- and Ce- based catalysts,[122–127] and other complex interfaces.[128,129]

With these insights, several important questions remain open. For instance, what is the molecular-level correlation between the behavior of the P1/P2 components and CO_2 reduction reactivity? How is the emergence and evolution of P1 modulated by local electric-field distortions arising from electrical double-layer (EDL) reorganization, such as interfacial water orientation or cation-specific adsorption or interactions? What precise geometric or electronic metrics create the twin peak phenomena and more generally, how relevant is the motif across various pathways of Cu surface restructuring? While these questions cannot be fully addressed with the present dataset, the observations reported here nevertheless point to broader implications for future SEIRAS studies of nanostructured catalysts. These distinctions underscore how the effects of coverage to skew surface selection rules, rather than adsorption geometry and site structure alone, can govern the spectral signatures observed. As molecular orientation of oscillators is also complicated by the nanograin architecture, what is the operative role, if any, that co-adsorbates elucidated from Raman may have in orientational effects of intermediates in the surface adlayer relative to the local field?

For vibrational modes that can couple via constructive or destructive interference, typically involving identical oscillators with similar frequencies, SEIRAS band intensities should not be interpreted as a direct measurement of adsorbate population or suggesting unique underlying structures. Moreover, the vibrational lineshape itself encodes information about nanoparticle-nanoparticle interactions, evolution state , and double-layer polarization. These encoded parameters may, in principle, be systematically disentangled through carefully designed and systematic SEIRAS protocols if the behavior of P1-P3 across different conditions can be further quantified and grounded. Although further validation is required, this underscores the promise of treating vibrational line shapes not merely as spectral features, but as reporters of a convolution or multitude of orchestrated phenomena, including increasing coverage, co-adsorbate dipole-dipole and non-covalent interactions, electronic coupling, and the strength of interfacial fields can, in sum, contribute to the observables at operating catalytic interfaces.

Downstream Intermediates on Cu Nanograins

With increased *CO accumulation, a representative pathway for C_{2+} formation may follow: CO_2 → *COOH → *CO → *optional* hydrogenation (*CHO or *COH) → C–C coupling i.e. *OC–CO^- → etc. *OCH–CH_2 → C_2H_4. CO signals will fluctuate based on reactivity. First, enhanced reactivity drives CO consumption via dimerization and hydrogenation, shortening its lifetime at the surface. Second, under high current densities, transport-limited CO_2 delivery leads to local depletion and competitive hydrogen adsorption, reducing CO coverage even as reactivity increases. In this regime, surface population is governed by reaction flux rather than adsorption equilibrium. The observed attenuation of CO therefore reflects a transition in the kinetic regime, not catalyst deactivation: CO is consumed faster than it accumulates as the potential becomes more negative. Beyond CO/$OCCO^-$, the exact identification of C_2 intermediates remains elusive because weak Raman cross sections, spectral overlap, and rapid turnover limit their detection. SERS sensitivity fails not because intermediates are intrinsically unstable, but because intermediates are also short-lived, dilute in snapshot measurements, and potentially weaker oscillators embedded in a crowded spectral field. Recent benchmarking using glyoxal as a molecular surrogate has provided important reference signatures for putative C–O/C-C vibrations in C_2 intermediates, revealing that characteristic bands of intermolecular modes of such intermediates span a broad window from ~1200 to 1975 cm^{-1} in SERS and SEIRAS.[130–133] Still, detection of downstream intermediates remains highly interpretive. These observations underscore the need for improved enhancement or deconvolution strategies, as well as complementary, higher-sensitivity spectroscopic methods. Alternatively, other strategies beyond vibrational spectroscopy can be explored to conclusively assign the molecular fingerprints of transient C_2 intermediates.[134–137]

Conclusion

This study highlights the nuanced interplay between surface coverage, co-adsorbate interactions, and nanostructure-derived field confinement in dictating the behavior of CO_2 reduction intermediates on Cu nanograin catalysts. While the core sequence of reaction steps remains broadly consistent with some prior reports, their manifestation is strongly modulated by local surface environments. Specifically, the mechanisms probed include Cu-carbonate surface adlayers at low overpotential, linear-atop *CO formation, and coexistence with persistent oxy- (*OH/*O) co-adsorbates. SERS and SEIRAS experiments indicate that electrolyte binding may gate stable CO binding at lower overpotentials, helping to, *in part*, rationalize the observed CO onset. Yet, a gap in activation suggests insufficient energy input is also a factor. Systematic shifts in CO stretching and frustrated rotational modes, from SERS, and isotherms corresponding to the CO bands, from SEIRAS, extend the previously reported coverage trends to the 6.7 nm Cu nanoparticle-derived nanograins.

This system underscores the role of dynamic surface ensembles in enhancing CO_2R selectivity. Two factors appear to be central to stabilizing dipolar Cu-*OH/O_x environments on Cu. Smaller nanograin domains intrinsically enhance *O/*OH binding. Second, elevated local pH, both kinetically and thermodynamically, preserves these motifs under reducing conditions in agreement with a complex Pourbaix diagram. In SEIRAS, the emergence of a P1/P2 'twin' feature, characterized by the rare splitting of linear CO modes, is emblematic of interfacial effects and underscores that nanograins host reactivity environments that are largely inaccessible to bulk-like Cu under comparable conditions (assuming no evolution). However, P1/P2 co-existence is also detected in SEIRAS spectra on Cu films and is fairly prominent in $CsHCO_3$ and not $KHCO_3$ conditions.

In sum, SEIRAS does more than confirm Raman assignments: it exposes how adsorbate coverage, double-layer fields, specific interactions, and local dielectric environment conspire to sculpt the CO line shapes. At present, it is not possible to unambiguously distinguish whether the evolution of the P1–P3 features reflects electric field-induced dipole stabilization within the interfacial region or changes in the local surface chemical state (e.g., *O/OH-mediated oxidation, reconstruction pathway, or re-orienting impact on neighboring species). Because these contributions are intrinsically coupled under electrochemical conditions, a single mechanistic origin is not assigned. These findings imply that, although mechanistic pathways remain largely intact across potential regimes, their spectral signatures are shaped by interfacial history, mass transport, nanoscale morphology, neighboring site motifs, surface diffusion, and coverage-dependent field effects.[78,138]

For downstream intermediates beyond CO, these data do not yet resolve the influence of nanograin morphology, though hints from the C–H stretching region in SEIRAS suggest that additional mechanistic detail beyond CO may be detectable. Clarifying modes from surface intermediates beyond CO represents an important direction for future studies. For example, while kinetic phenomena, including rate-limiting steps, maintain restrictions on which intermediates can be observed more easily than others, specific strategies have been introduced to enhance mechanistic

insight, such as feeding downstream intermediates (CO, formaldehyde, glyoxal) or operating at high current densities to boost the total concentration of specific reaction steps to a detectable threshold.[139,140] Another proposed mitigation is to conduct Raman measurements under elevated CO_2 pressure to reduce CO_2 mass-transport limitations and therefore extend CO residence times.[6,132,141] This will have the concurrent effect to further diminish competing HER reactions, allowing higher *CO coverage regimes and related pathways to be explored.

Ultimately, vibrational spectroscopy cannot, on its own, resolve every ambiguity in this mechanism. Progress toward mechanistic quantitation requires a decisive shift away from a static spectral snapshot. These, while valuable, cannot fully capture the kinetic choreography of intermediates and fields that unfold across time and potential. Mainly, what remains lacking is access to emergent pathways, which can be further promoted with the developing understanding of Cu surface chemistry under catalytic operation. To this end, linking the physiochemical interplay of such motifs on the underlying Cu surface phase is an exciting direction of follow-on studies. To advance mechanistic quantification, proposed methods must therefore be judged by their compatibility with reproducing reaction environments and their capacity to yield unambiguous mechanistic insight, ideally under time-resolved interrogation. Yet, a departure from static to dynamic analysis demands overcoming significant practical challenges. It involves synchronizing modulation frequencies, improving detection sensitivity, and developing advanced algorithms to disentangle overlapping spectral signals and the evolving nature of the catalytic interface that obscures remaining interpretations of surface chemistry.[142] With this approach, vibrational techniques could unlock an even deeper understanding, moving us closer to a predictive framework that reveals pre-equilibria, pinpoints how catalyst structure and interfacial dynamics intersect, and helps encode the two to achieve controlled chemical outcomes.[143,144] This remains essential for resolving behaviors across the broad spectrum of pH and electrolyte composition relevant for CO_2R. Interfacial environments and dominant surface species can shift dramatically between acidic and basic aqueous electrolytes, as well as in mixed-solvent environments (addition of DMSO, acetonitrile), each contributing to acute catalytic bottlenecks that remain to be broadly elucidated.[8,145–147] To achieve this, we can polish our spectroscopic lens and aim to capture the buildup, depletion, and pairing of interfacial species with sufficient temporal fidelity.

Collectively, these results support a view of nanograin Cu not as a collection of isolated active sites, but as a dynamically reorganizing interface in which intermediate and co-adsorbate coverage, interfacial confinement, local pH, and field effects are inseparable. Rather than attributing selectivity to isolated structural motifs, we propose that nanograin catalysts operate in a regime in which surface coverage and crowding, interfacial electric fields, and repopulating low-coordination structural motifs jointly govern reaction pathways. In this picture, selectivity therefore arises from a dynamic balance between favoring atop CO intermediates, co-adsorbate stabilization and mobility, rather than from static binding energies alone. This secures a pathway toward more mechanistically resolved interpretation of *operando* spectroscopy. By leveraging the outcome or balance of these contributions in pre-catalyst design, we can provide a foundation for optimized CO_2R catalyst design grounded in interfacial dynamics.

References

(1) Nitopi, S.; Bertheussen, E.; Scott, S. B.; Liu, X.; Engstfeld, A. K.; Horch, S.; Seger, B.; Stephens, I. E. L.; Chan, K.; Hahn, C.; Nørskov, J. K.; Jaramillo, T. F.; Chorkendorff, I. Progress and Perspectives of Electrochemical CO2 Reduction on Copper in Aqueous Electrolyte. *Chem. Rev.* **2019**, *119* (12), 7610–7672. https://doi.org/10.1021/acs.chemrev.8b00705.

(2) Kuhl, K. P.; Cave, E. R.; Abram, D. N.; Jaramillo, T. F. New Insights into the Electrochemical Reduction of Carbon Dioxide on Metallic Copper Surfaces. *Energy Environ. Sci.* **2012**, *5* (5), 7050–7059.

(3) Costentin, C.; Robert, M.; Savéant, J.-M.; Tatin, A. Efficient and Selective Molecular Catalyst for the CO2-to-CO Electrochemical Conversion in Water. *Proc. Natl. Acad. Sci.* **2015**, *112* (22), 6882–6886.

(4) Kim, D.; Yu, S.; Zheng, F.; Roh, I.; Li, Y.; Louisia, S.; Qi, Z.; Somorjai, G. A.; Frei, H.; Wang, L.-W. Selective CO2 Electrocatalysis at the Pseudocapacitive Nanoparticle/Ordered-Ligand Interlayer. *Nat. Energy* **2020**, *5* (12), 1032–1042.

(5) Peng, H.-J.; Tang, M. T.; Halldin Stenlid, J.; Liu, X.; Abild-Pedersen, F. Trends in Oxygenate/Hydrocarbon Selectivity for Electrochemical CO(2) Reduction to C2 Products. *Nat. Commun.* **2022**, *13* (1), 1399. https://doi.org/10.1038/s41467-022-29140-8.

(6) Vos, R. E.; Sun, P.; Schauermann, D.; Javed, H.; Hanselman, S. R.; Fu, G.; Koper, M. T. CO2 Electroreduction on Cu Operates via an Alternative Chain Growth Mechanism to Form C–C Bonds at Elevated Temperature and Pressure. *Nat. Catal.* **2025**, 1–10.

(7) Fang, M.; Wang, M.; Wang, Z.; Zhang, Z.; Zhou, H.; Dai, L.; Zhu, Y.; Jiang, L. Hydrophobic, Ultrastable Cuδ+ for Robust CO2 Electroreduction to C2 Products at Ampere-Current Levels. *J. Am. Chem. Soc.* **2023**, *145* (20), 11323–11332.

(8) García de Arquer, F. P.; Dinh, C.-T.; Ozden, A.; Wicks, J.; McCallum, C.; Kirmani, A. R.; Nam, D.-H.; Gabardo, C.; Seifitokaldani, A.; Wang, X.; Li, Y. C.; Li, F.; Edwards, J.; Richter, L. J.; Thorpe, S. J.; Sinton, D.; Sargent, E. H. CO2 Electrolysis to Multicarbon Products at Activities Greater than 1 A Cm−2. *Science* **2020**, *367* (6478), 661–666. https://doi.org/10.1126/science.aay4217.

(9) De Ruiter, J.; Benning, V. R. M.; Yang, S.; den Hartigh, B. J.; Wang, H.; Prins, P. T.; Dorresteijn, J. M.; Janssens, J. C. L.; Manna, G.; Petukhov, A. V. Multiscale X-Ray Scattering Elucidates Activation and Deactivation of Oxide-Derived Copper Electrocatalysts for CO2 Reduction. *Nat. Commun.* **2025**, *16* (1), 373.

(10) Kok, J.; Albertini, P. P.; Leemans, J.; Buonsanti, R.; Burdyny, T. Overcoming Copper Stability Challenges in CO2 Electrolysis. *Nat. Rev. Mater.* **2025**, *10* (7), 550–563. https://doi.org/10.1038/s41578-025-00815-0.

(11) Shan, Y.; Zhao, X.; Fonseca Guzman, M.; Jana, A.; Chen, S.; Yu, S.; Ng, K. C.; Roh, I.; Chen, H.; Altoe, V. Nanometre-Resolved Observation of Electrochemical Microenvironment Formation at the Nanoparticle–Ligand Interface. *Nat. Catal.* **2024**, *7* (4), 422–431.

(12) Wei, J.; Zhang, Z.; Gee, W.; Wei, Y.; Zhou, Y.-W.; Herran, M.; Sautet, P.; Alexandrova, A. N.; Roldan Cuenya, B.; Kley, C. S. Role of Surface Hydroxyls in Atomic-Scale Copper Restructuring during CO Electroreduction. *J. Am. Chem. Soc.* **2025**, *147* (49), 45178–45188. https://doi.org/10.1021/jacs.5c14516.

(13) Zhang, Y.; Chen, Y.; Wang, X.; Feng, Y.; Dai, Z.; Cheng, M.; Zhang, G. Low-Coordinated Copper Facilitates The* CH2CO Affinity at Enhanced Rectifying Interface of Cu/Cu2O for Efficient CO2-to-Multicarbon Alcohols Conversion. *Nat. Commun.* **2024**, *15* (1), 5172.

(14) Cai, J.; Zhao, Q.; Hsu, W.-Y.; Choi, C.; Liu, Y.; Martirez, J. M. P.; Chen, C.; Huang, J.; Carter, E. A.; Huang, Y. Highly Selective Electrochemical Reduction of CO2 into Methane on Nanotwinned Cu. *J. Am. Chem. Soc.* **2023**, *145* (16), 9136–9143.

(15) Cheng, D.; Nguyen, K.-L. C.; Sumaria, V.; Wei, Z.; Zhang, Z.; Gee, W.; Li, Y.; Morales-Guio, C. G.; Heyde, M.; Roldan Cuenya, B. Structure Sensitivity and Catalyst Restructuring for CO2 Electro-Reduction on Copper. *Nat. Commun.* **2025**, *16* (1), 4064.

(16) Yang, Y.; Feijóo, J.; Figueras-Valls, M.; Chen, C.; Shi, C.; Fonseca Guzman, M. V.; Murhabazi Maombi, Y.; Liu, S.; Jain, P.; Briega-Martos, V. Operando Probing Dynamic Migration of Copper Carbonyl during Electrocatalytic CO2 Reduction. *Nat. Catal.* **2025**, *8* (6), 579–594.

(17) Huang, J.; Hörmann, N.; Oveisi, E.; Loiudice, A.; De Gregorio, G. L.; Andreussi, O.; Marzari, N.; Buonsanti, R. Potential-Induced Nanoclustering of Metallic Catalysts during Electrochemical CO2 Reduction. *Nat. Commun.* **2018**, *9* (1), 3117.

(18) You, X.; Baiz, C. R. Importance of Hydrogen Bonding in Crowded Environments: A Physical Chemistry Perspective. *J. Phys. Chem. A* **2022**, *126* (35), 5881–5889. https://doi.org/10.1021/acs.jpca.2c03803.

(19) Arán-Ais, R. M.; Scholten, F.; Kunze, S.; Rizo, R.; Roldan Cuenya, B. The Role of in Situ Generated Morphological Motifs and Cu(i) Species in C2+ Product Selectivity during CO2 Pulsed Electroreduction. *Nat. Energy* **2020**, *5* (4), 317–325. https://doi.org/10.1038/s41560-020-0594-9.

(20) Zhong, D.; Cheng, D.; Fang, Q.; Liu, Y.; Li, J.; Zhao, Q. Understanding the Restructuring and Degradation of Oxide-Derived Copper during Electrochemical CO2 Reduction. *Chem. Eng. J.* **2023**, *470*, 143907. https://doi.org/10.1016/j.cej.2023.143907.

(21) Cheng, D.; Zhao, Z.-J.; Zhang, G.; Yang, P.; Li, L.; Gao, H.; Liu, S.; Chang, X.; Chen, S.; Wang, T.; Ozin, G. A.; Liu, Z.; Gong, J. The Nature of Active Sites for Carbon Dioxide Electroreduction over Oxide-Derived Copper Catalysts. *Nat. Commun.* **2021**, *12* (1), 395. https://doi.org/10.1038/s41467-020-20615-0.

(22) Pang, Y.; Li, J.; Wang, Z.; Tan, C.-S.; Hsieh, P.-L.; Zhuang, T.-T.; Liang, Z.-Q.; Zou, C.; Wang, X.; De Luna, P.; Edwards, J. P.; Xu, Y.; Li, F.; Dinh, C.-T.; Zhong, M.; Lou, Y.; Wu, D.; Chen, L.-J.; Sargent, E. H.; Sinton, D. Efficient Electrocatalytic Conversion of Carbon Monoxide to Propanol Using Fragmented Copper. *Nat. Catal.* **2019**, *2* (3), 251–258. https://doi.org/10.1038/s41929-019-0225-7.

(23) Yang, Y.; Shi, C.; Feijóo, J.; Jin, J.; Chen, C.; Han, Y.; Yang, P. Dynamic Evolution of Copper Nanowires during CO2 Reduction Probed by Operando Electrochemical 4D-STEM and X-Ray Spectroscopy. *J. Am. Chem. Soc.* **2024**, *146* (33), 23398–23405. https://doi.org/10.1021/jacs.4c06480.

(24) Yang, Y.; Louisia, S.; Yu, S.; Jin, J.; Roh, I.; Chen, C.; Fonseca Guzman, M. V.; Feijóo, J.; Chen, P.-C.; Wang, H.; Pollock, C. J.; Huang, X.; Shao, Y.-T.; Wang, C.; Muller, D. A.; Abruña, H. D.; Yang, P. Operando Studies Reveal Active Cu Nanograins for CO2 Electroreduction. *Nature* **2023**, *614* (7947), 262–269. https://doi.org/10.1038/s41586-022-05540-0.

(25) Jing, S.; Wang, G.; Li, Z.; Xiao, W.; Zhuang, L. Maintaining Local Alkalinity of CO-Electroreduction Full Cell by Silica-Confined Electrocatalysts in Membrane Electrode Assembly. *Sci. Adv.* **2025**, *11* (48), eaeb3478. https://doi.org/10.1126/sciadv.aeb3478.

(26) Kumar, A. S.; Pupo, M.; Petrov, K. V.; Ramdin, M.; van Ommen, J. R.; de Jong, W.; Kortlever, R. A Quantitative Analysis of Electrochemical CO2 Reduction on Copper in Organic Amide and Nitrile-Based Electrolytes. *J. Phys. Chem. C* **2023**, *127* (27), 12857–12866. https://doi.org/10.1021/acs.jpcc.3c01955.

(27) Hao, Q.; Liu, D.-X.; Zhong, H.-X.; Tang, Q.; Yan, J.-M. Electrocatalytic CO2 Reduction in Acidic Medium. *Chem Catal.* **2023**, *3* (3), 100542. https://doi.org/10.1016/j.checat.2023.100542.

(28) Ge, W.; Zhu, Y.; Wang, H.; Jiang, H.; Li, C. Anionic Surfactant-Tuned Interfacial Water Reactivity Promoting Electrocatalytic CO2 Reduction. *ACS Catal.* **2024**, *14* (23), 18156–18166. https://doi.org/10.1021/acscatal.4c05541.

(29) Mondal, S.; Chen, K.; Baiz, C. Cosolvents Disrupt Water H-Bond Networks at Electrode Interfaces: A Surface-Enhanced 2D IR Study. ChemRxiv November 3, 2025. https://doi.org/10.26434/chemrxiv-2025-4jhpf-v2.

(30) Peng, B.; Liu, Z.; Ma, X.; Ni, W.; Shah, A. H.; Musgrave, C. B.; Park, H.; Huang, J.; Menon, A.; Kanatzidis, M. G.; Xie, K.; Sargent, E. H. A Cation-Functionalized Layer for Ethylene Electrosynthesis via CO Reduction Paired with H2 Oxidation in a Pure-Water-Fed Solid-State Electrolyser. *Nat. Energy* **2026**, 1–10. https://doi.org/10.1038/s41560-026-01990-2.

(31) Bui, J. C.; Kim, C.; Weber, A. Z.; Bell, A. T. Dynamic Boundary Layer Simulation of Pulsed CO2 Electrolysis on a Copper Catalyst. *ACS Energy Lett.* **2021**, *6* (4), 1181–1188. https://doi.org/10.1021/acsenergylett.1c00364.

(32) Louisia, S.; Kim, D.; Li, Y.; Gao, M.; Yu, S.; Roh, I.; Yang, P. The Presence and Role of the Intermediary CO Reservoir in Heterogeneous Electroreduction of CO2. *Proc. Natl. Acad. Sci.* **2022**, *119* (18), e2201922119. https://doi.org/10.1073/pnas.2201922119.

(33) Kim, D.; Kley, C. S.; Li, Y.; Yang, P. Copper Nanoparticle Ensembles for Selective Electroreduction of CO2 to C2–C3 Products. *Proc. Natl. Acad. Sci.* **2017**, *114* (40), 10560–10565. https://doi.org/10.1073/pnas.1711493114.

(34) Li, Y.; Kim, D.; Louisia, S.; Xie, C.; Kong, Q.; Yu, S.; Lin, T.; Aloni, S.; Fakra, S. C.; Yang, P. Electrochemically Scrambled Nanocrystals Are Catalytically Active for CO2-to-Multicarbons. *Proc. Natl. Acad. Sci.* **2020**, *117* (17), 9194–9201. https://doi.org/10.1073/pnas.1918602117.

(35) Leemans, J.; Fako, E.; Zaza, L.; Tritschler, M.; Chen, J.; Schwaller, P.; Buonsanti, R. Ligand-Modulated Release of Copper Active Sites Extends Ethylene Production in CO2 Electroreduction. *J. Am. Chem. Soc.* **2026**, *148* (12), 13118–13127. https://doi.org/10.1021/jacs.5c22701.

(36) Varley, J. B.; Govindarajan, N.; Ager, J. W. Understanding the Unique Reactivity of Cu for Electrochemical CO2 Reduction with a 3-Site Model. *J. Phys. Chem. Lett.* **2025**, *16* (2), 604–610. https://doi.org/10.1021/acs.jpclett.4c03157.

(37) Houle, F. A.; Agbo, P.; Yano, J. Insights from Designing an Artificial Cascade Catalysis System Using Principles from Substrate Channeling in Enzymes. *Chem Sci* **2025**, *16*, 13667–13677. https://doi.org/10.1039/D5SC02781K.

(38) Birdja, Y. Y.; Pérez-Gallent, E.; Figueiredo, M. C.; Göttle, A. J.; Calle-Vallejo, F.; Koper, M. T. M. Advances and Challenges in Understanding the Electrocatalytic Conversion of Carbon Dioxide to Fuels. *Nat. Energy* **2019**, *4* (9), 732–745. https://doi.org/10.1038/s41560-019-0450-y.

(39) Kelly, K. L.; Coronado, E.; Zhao, L. L.; Schatz, G. C. The Optical Properties of Metal Nanoparticles: The Influence of Size, Shape, and Dielectric Environment. *J. Phys. Chem. B* **2003**, *107* (3), 668–677. https://doi.org/10.1021/jp026731y.

(40) dos Santos, D. P.; Temperini, M. L. A.; Brolo, A. G. Intensity Fluctuations in Single-Molecule Surface-Enhanced Raman Scattering. *Acc. Chem. Res.* **2019**, *52* (2), 456–464. https://doi.org/10.1021/acs.accounts.8b00563.

(41) Linic, S.; Chavez, S.; Elias, R. Flow and Extraction of Energy and Charge Carriers in Hybrid Plasmonic Nanostructures. *Nat. Mater.* **2021**, *20* (7), 916–924. https://doi.org/10.1038/s41563-020-00858-4.

(42) *Surface-Enhanced Raman Scattering*; Kneipp, K., Moskovits, M., Kneipp, H., Eds.; Topics in Applied Physics; Springer Berlin Heidelberg, 2006; Vol. 103. https://doi.org/10.1007/3-540-33567-6.

(43) Kuhl, K. P.; Hatsukade, T.; Cave, E. R.; Abram, D. N.; Kibsgaard, J.; Jaramillo, T. F. Electrocatalytic Conversion of Carbon Dioxide to Methane and Methanol on Transition Metal Surfaces. *J. Am. Chem. Soc.* **2014**, *136* (40), 14107–14113. https://doi.org/10.1021/ja505791r.

(44) Chen, Y.; Li, C. W.; Kanan, M. W. Aqueous CO2 Reduction at Very Low Overpotential on Oxide-Derived Au Nanoparticles. *J. Am. Chem. Soc.* **2012**, *134* (49), 19969–19972. https://doi.org/10.1021/ja309317u.

(45) Herzog, A.; Lopez Luna, M.; Jeon, H. S.; Rettenmaier, C.; Grosse, P.; Bergmann, A.; Roldan Cuenya, B. Operando Raman Spectroscopy Uncovers Hydroxide and CO Species Enhance Ethanol Selectivity during Pulsed CO2 Electroreduction. *Nat. Commun.* **2024**, *15* (1), 3986. https://doi.org/10.1038/s41467-024-48052-3.

(46) Moradzaman, M.; Mul, G. In Situ Raman Study of Potential-Dependent Surface Adsorbed Carbonate, CO, OH, and C Species on Cu Electrodes During Electrochemical Reduction of CO2. *ChemElectroChem* **2021**, *8* (8), 1478–1485. https://doi.org/10.1002/celc.202001598.

(47) Henckel, D. A.; Counihan, M. J.; Holmes, H. E.; Chen, X.; Nwabara, U. O.; Verma, S.; Rodríguez-López, J.; Kenis, P. J. A.; Gewirth, A. A. Potential Dependence of the Local pH in a CO2 Reduction Electrolyzer. *ACS Catal.* **2021**, *11* (1), 255–263. https://doi.org/10.1021/acscatal.0c04297.

(48) Kim, J.; Lee, S. Y.; Kim, S.-J.; Koo, B.; Chung, J.; Lee, D.; Choi, S.; Kim, J.; Seo, S.; Nam, C.; Gandionco, K. A.; Bak, G.; Jo, S.; Kim, N.; Shin, H.-J.; Chae, K. H.; Won, D. H.; Marcus, M. A.; Shapiro, D. A.; Haw, S.-C.; Alsem, D. H.; Salmon, N. J.; Min, B. K.; Kim, H.; Hwang, Y. J.; Lim, J. Spatiotemporal Active Phase Evolution for CO2 Electrocatalysis. *Joule* **2024**, *8* (12), 3373–3385. https://doi.org/10.1016/j.joule.2024.09.008.

(49) Ma, H.; Ibáñez-Alé, E.; Ganganahalli, R.; Pérez-Ramírez, J.; López, N.; Yeo, B. S. Direct Electroreduction of Carbonate to Formate. *J. Am. Chem. Soc.* **2023**, *145* (45), 24707–24716. https://doi.org/10.1021/jacs.3c08079.

(50) de Ruiter, J.; An, H.; Wu, L.; Gijsberg, Z.; Yang, S.; Hartman, T.; Weckhuysen, B. M.; van der Stam, W. Probing the Dynamics of Low-Overpotential CO2-to-CO Activation on Copper Electrodes with Time-Resolved Raman Spectroscopy. *J. Am. Chem. Soc.* **2022**, *144* (33), 15047–15058. https://doi.org/10.1021/jacs.2c03172.

(51) Yoo, J. M.; Ingenmey, J.; Salanne, M.; Lukatskaya, M. R. Anion Effect in Electrochemical CO2 Reduction: From Spectators to Orchestrators. *J. Am. Chem. Soc.* **2024**, *146* (46), 31768–31777. https://doi.org/10.1021/jacs.4c10661.

(52) Shao, F.; Wong, J. K.; Low, Q. H.; Iannuzzi, M.; Li, J.; Lan, J. In Situ Spectroelectrochemical Probing of CO Redox Landscape on Copper Single-Crystal Surfaces. *Proc. Natl. Acad. Sci.* **2022**, *119* (29), e2118166119. https://doi.org/10.1073/pnas.2118166119.

(53) Jiang, S.; D'Amario, L.; Dau, H. Copper Carbonate Hydroxide as Precursor of Interfacial CO in CO2 Electroreduction. *ChemSusChem* **2022**, *15* (8), e202102506. https://doi.org/10.1002/cssc.202102506.

(54) Pérez-Gallent, E.; Marcandalli, G.; Figueiredo, M. C.; Calle-Vallejo, F.; Koper, M. T. M. Structure- and Potential-Dependent Cation Effects on CO Reduction at Copper Single-Crystal Electrodes. *J. Am. Chem. Soc.* **2017**, *139* (45), 16412–16419. https://doi.org/10.1021/jacs.7b10142.

(55) Amirbeigiarab, R.; Tian, J.; Herzog, A.; Qiu, C.; Bergmann, A.; Roldan Cuenya, B.; Magnussen, O. M. Atomic-Scale Surface Restructuring of Copper Electrodes under CO2 Electroreduction Conditions. *Nat. Catal.* **2023**, *6* (9), 837–846. https://doi.org/10.1038/s41929-023-01009-z.

(56) Munz, M.; Poon, J.; Frandsen, W.; Cuenya, B. R.; Kley, C. S. Nanoscale Electron Transfer Variations at Electrocatalyst–Electrolyte Interfaces Resolved by in Situ Conductive Atomic Force Microscopy. *J. Am. Chem. Soc.* **2023**, *145* (9), 5242–5251. https://doi.org/10.1021/jacs.2c12617.

(57) Zang, J.; Ye, W.; Liu, Q.; Meng, J.; Yang, W. Plasmonic-Promoted Formation of Surface Adsorbed Stochastic CO during Electrochemical CO2 and CO Reduction on Cu at Extreme Low Overpotentials. *J. Am. Chem. Soc.* **2025**, *147* (12), 10260–10267. https://doi.org/10.1021/jacs.4c16579.

(58) Amirbeigiarab, R.; Bagger, A.; Tian, J.; Rossmeisl, J.; Magnussen, O. M. Structure of the (Bi)Carbonate Adlayer on Cu(100) Electrodes. *Angew. Chem. Int. Ed.* **2022**, *61* (46), e202211360. https://doi.org/10.1002/anie.202211360.

(59) Zhan, C.; Dattila, F.; Rettenmaier, C.; Bergmann, A.; Kühl, S.; García-Muelas, R.; López, N.; Cuenya, B. R. Revealing the CO Coverage-Driven C–C Coupling Mechanism for Electrochemical CO2 Reduction on Cu2O Nanocubes via Operando Raman Spectroscopy. *ACS Catal.* **2021**, *11* (13), 7694–7701. https://doi.org/10.1021/acscatal.1c01478.

(60) Wuttig, A.; Ryu, J.; Surendranath, Y. Electrolyte Competition Controls Surface Binding of CO Intermediates to CO2 Reduction Catalysts. *J. Phys. Chem. C* **2021**, *125* (31), 17042–17050. https://doi.org/10.1021/acs.jpcc.1c04337.

(61) Meng, J.; Freeze, J.; Nowack, L.; Li, C.; Wang, H.; Abruña, H. D.; Willard, A. P.; Batista, V. S.; Lian, T. Competitive Carbonate Binding Hinders Electrochemical CO2 Reduction to CO on Cu Surfaces at Low Overpotentials. *J. Am. Chem. Soc.* **2025**, *147* (29), 25361–25371. https://doi.org/10.1021/jacs.5c04518.

(62) Zhang, Z.-M.; Wang, T.; Cai, Y.-C.; Li, X.-Y.; Ye, J.-Y.; Zhou, Y.; Tian, N.; Zhou, Z.-Y.; Sun, S.-G. Probing Electrolyte Effects on Cation-Enhanced CO2 Reduction on Copper in Acidic Media. *Nat. Catal.* **2024**, *7* (7), 807–817. https://doi.org/10.1038/s41929-024-01179-4.

(63) An, H.; de Ruiter, J.; Wu, L.; Yang, S.; Meirer, F.; van der Stam, W.; Weckhuysen, B. M. Spatiotemporal Mapping of Local Heterogeneities during Electrochemical Carbon Dioxide Reduction. *JACS Au* **2023**, *3* (7), 1890–1901. https://doi.org/10.1021/jacsau.3c00129.

(64) Zhong, D.; Fang, Q.; Du, R.; Jin, Y.; Peng, C.; Cheng, D.; Li, T.; Zhao, T.; Zhang, S.; Zheng, Y.; Zhao, Q.; Sun, Y.; Li, J. Selective Electrochemical CO2 Reduction to Ethylene or Ethanol via Tuning *OH Adsorption. *Angew. Chem. Int. Ed.* **2025**, *64* (32), e202501773. https://doi.org/10.1002/anie.202501773.

(65) Liu, Q.; Zang, J.; Ye, W.; Li, L.; Wang, C.; Jin, J.; Yang, W. Universal Formation, Dynamics, and Reactivities of *CObridge Accompanying Spontaneous Reconstruction of Cu during Electrochemical CO2 or CO Reduction. *J. Am. Chem. Soc.* **2025**, *147* (35), 31497–31508. https://doi.org/10.1021/jacs.5c03886.

(66) Li, J.; Chang, X.; Zhang, H.; Malkani, A. S.; Cheng, M.; Xu, B.; Lu, Q. Electrokinetic and in Situ Spectroscopic Investigations of CO Electrochemical Reduction on Copper. *Nat. Commun.* **2021**, *12* (1), 3264. https://doi.org/10.1038/s41467-021-23582-2.

(67) Ma, H.; Ibáñez-Alé, E.; You, F.; López, N.; Yeo, B. S. Electrochemical Formation of C2+ Products Steered by Bridge-Bonded *CO Confined by *OH Domains. *J. Am. Chem. Soc.* **2024**, *146* (44), 30183–30193. https://doi.org/10.1021/jacs.4c08755.

(68) Magnussen, O. M.; Groß, A. Toward an Atomic-Scale Understanding of Electrochemical Interface Structure and Dynamics. *J. Am. Chem. Soc.* **2019**, *141* (12), 4777–4790. https://doi.org/10.1021/jacs.8b13188.

(69) Rossmeisl, J.; Nørskov, J. K.; Taylor, C. D.; Janik, M. J.; Neurock, M. Calculated Phase Diagrams for the Electrochemical Oxidation and Reduction of Water over Pt(111). *J. Phys. Chem. B* **2006**, *110* (43), 21833–21839. https://doi.org/10.1021/jp0631735.

(70) Hammes-Schiffer, S.; Soudackov, A. V. Proton-Coupled Electron Transfer in Solution, Proteins, and Electrochemistry. *J. Phys. Chem. B* **2008**, *112* (45), 14108–14123. https://doi.org/10.1021/jp805876e.

(71) Bohra, D.; Ledezma-Yanez, I.; Li, G.; de Jong, W.; Pidko, E. A.; Smith, W. A. Lateral Adsorbate Interactions Inhibit HCOO− While Promoting CO Selectivity for CO2 Electrocatalysis on Silver. *Angew. Chem. Int. Ed.* **2019**, *58* (5), 1345–1349. https://doi.org/10.1002/anie.201811667.

(72) Zou, T.; Veenstra, F. L. P.; Ibáñez-Alé, E.; García-Muelas, R.; Zichittella, G.; Martín, A. J.; López, N.; Pérez-Ramírez, J. Chlorine-Promoted Copper Catalysts for CO2 Electroreduction into Highly Reduced Products. *Cell Rep. Phys. Sci.* **2023**, *4* (3), 101294. https://doi.org/10.1016/j.xcrp.2023.101294.

(73) Zhang, L.; Feng, J.; Wu, L.; Ma, X.; Song, X.; Jia, S.; Tan, X.; Jin, X.; Zhu, Q.; Kang, X.; Ma, J.; Qian, Q.; Zheng, L.; Sun, X.; Han, B. Oxophilicity-Controlled CO2 Electroreduction to C2+ Alcohols over Lewis Acid Metal-Doped Cuδ+ Catalysts. *J. Am. Chem. Soc.* **2023**, *145* (40), 21945–21954. https://doi.org/10.1021/jacs.3c06697.

(74) Baldenebro-López, J.; Castorena-González, J.; Flores-Holguín, N.; Almaral-Sánchez, J.; Glossman-Mitnik, D. Computational Molecular Nanoscience Study of the Properties of Copper Complexes for Dye-Sensitized Solar Cells. *Int. J. Mol. Sci.* **2012**, *13* (12), 16005–16019. https://doi.org/10.3390/ijms131216005.

(75) Chan, K. A Few Basic Concepts in Electrochemical Carbon Dioxide Reduction. *Nat. Commun.* **2020**, *11* (1), 5954. https://doi.org/10.1038/s41467-020-19369-6.

(76) Lian, Z.; Dattila, F.; López, N. Stability and Lifetime of Diffusion-Trapped Oxygen in Oxide-Derived Copper CO2 Reduction Electrocatalysts. *Nat. Catal.* **2024**, *7* (4), 401–411. https://doi.org/10.1038/s41929-024-01132-5.

(77) Poberžnik, M.; Kokalj, A. Surprising Lateral Interactions between Negatively Charged Adatoms on Metal Surfaces. *J. Phys. Chem. Lett.* **2020**, *11* (17), 7122–7126. https://doi.org/10.1021/acs.jpclett.0c01373.

(78) Yang, K.; Kas, R.; Smith, W. A. In Situ Infrared Spectroscopy Reveals Persistent Alkalinity near Electrode Surfaces during CO2 Electroreduction. *J. Am. Chem. Soc.* **2019**, *141* (40), 15891–15900. https://doi.org/10.1021/jacs.9b07000.

(79) Yao, K.; Li, J.; Ozden, A.; Wang, H.; Sun, N.; Liu, P.; Zhong, W.; Zhou, W.; Zhou, J.; Wang, X.; Liu, H.; Liu, Y.; Chen, S.; Hu, Y.; Wang, Z.; Sinton, D.; Liang, H. In Situ Copper Faceting Enables Efficient CO2/CO Electrolysis. *Nat. Commun.* **2024**, *15* (1), 1749. https://doi.org/10.1038/s41467-024-45538-y.

(80) Herzog, A.; Lopez Luna, M.; Jeon, H. S.; Rettenmaier, C.; Grosse, P.; Bergmann, A.; Roldan Cuenya, B. Operando Raman Spectroscopy Uncovers Hydroxide and CO Species Enhance Ethanol Selectivity during Pulsed CO2 Electroreduction. *Nat. Commun.* **2024**, *15* (1), 3986. https://doi.org/10.1038/s41467-024-48052-3.

(81) Zhan, C.; Dattila, F.; Rettenmaier, C.; Herzog, A.; Herran, M.; Wagner, T.; Scholten, F.; Bergmann, A.; López, N.; Roldan Cuenya, B. Key Intermediates and Cu Active Sites for CO2 Electroreduction to Ethylene and Ethanol. *Nat. Energy* **2024**, *9* (12), 1485–1496. https://doi.org/10.1038/s41560-024-01633-4.

(82) Ye, Y.; Yang, H.; Qian, J.; Su, H.; Lee, K.-J.; Cheng, T.; Xiao, H.; Yano, J.; Goddard, W. A.; Crumlin, E. J. Dramatic Differences in Carbon Dioxide Adsorption and Initial Steps of Reduction between Silver and Copper. *Nat. Commun.* **2019**, *10* (1), 1875. https://doi.org/10.1038/s41467-019-09846-y.

(83) Groppo, E.; Rojas-Buzo, S.; Bordiga, S. The Role of In Situ/Operando IR Spectroscopy in Unraveling Adsorbate-Induced Structural Changes in Heterogeneous Catalysis. *Chem. Rev.* **2023**, *123* (21), 12135–12169. https://doi.org/10.1021/acs.chemrev.3c00372.

(84) Chang, X.; Vijay, S.; Zhao, Y.; Oliveira, N. J.; Chan, K.; Xu, B. Understanding the Complementarities of Surface-Enhanced Infrared and Raman Spectroscopies in CO Adsorption and Electrochemical Reduction. *Nat. Commun.* **2022**, *13* (1), 2656. https://doi.org/10.1038/s41467-022-30262-2.

(85) Kozuch, J.; Ataka, K.; Heberle, J. Surface-Enhanced Infrared Absorption Spectroscopy. *Nat. Rev. Methods Primer* **2023**, *3* (1), 70. https://doi.org/10.1038/s43586-023-00253-8.

(86) Wang, Y.; Ding, J.; Su, C.; Shen, Z.; Liu, B. ATR-SEIRAS for Single-Atom Electrocatalysis. *Acc. Chem. Res.* **2025**, *58* (14), 2282–2295. https://doi.org/10.1021/acs.accounts.5c00303.

(87) Cuesta, A. ATR-SEIRAS for Time-Resolved Studies of Electrode–Electrolyte Interfaces. *Curr. Opin. Electrochem.* **2022**, *35*, 101041. https://doi.org/10.1016/j.coelec.2022.101041.

(88) Feijóo, J.; Yang, Y.; Fonseca Guzman, M. V.; Vargas, A.; Chen, C.; Pollock, C. J.; Yang, P. Operando High-Energy-Resolution X-Ray Spectroscopy of Evolving Cu Nanoparticle Electrocatalysts for CO2 Reduction. *J. Am. Chem. Soc.* **2023**, *145* (37), 20208–20213. https://doi.org/10.1021/jacs.3c08182.

(89) Delmo, E. P.; Wang, Y.; Song, Y.; Zhu, S.; Zhang, H.; Xu, H.; Li, T.; Jang, J.; Kwon, Y.; Wang, Y.; Shao, M. In Situ Infrared Spectroscopic Evidence of Enhanced Electrochemical CO2 Reduction and C–C Coupling on Oxide-Derived Copper. *J. Am. Chem. Soc.* **2024**, *146* (3), 1935–1945. https://doi.org/10.1021/jacs.3c08927.

(90) Gunathunge, C. M.; Ovalle, V. J.; Li, Y.; Janik, M. J.; Waegele, M. M. Existence of an Electrochemically Inert CO Population on Cu Electrodes in Alkaline pH. *ACS Catal.* **2018**, *8* (8), 7507–7516. https://doi.org/10.1021/acscatal.8b01552.

(91) Gunathunge, C. M.; Li, X.; Li, J.; Hicks, R. P.; Ovalle, V. J.; Waegele, M. M. Spectroscopic Observation of Reversible Surface Reconstruction of Copper Electrodes under CO2 Reduction. *J. Phys. Chem. C* **2017**, *121* (22), 12337–12344. https://doi.org/10.1021/acs.jpcc.7b03910.

(92) Su, Z.-F.; Sun, S.-G.; Wu, C.-X.; Cai, Z.-P. Study of Anomalous Infrared Properties of Nanomaterials through Effective Medium Theory. *J. Chem. Phys.* **2008**, *129* (4), 044707. https://doi.org/10.1063/1.2953441.

(93) Wu, C.-X.; Lin, H.; Chen, Y.-J.; Li, W.-X.; Sun, S.-G. Abnormal IR Effects of Pt Nanostructured Surfaces upon CO Chemisorption Due to Interaction and Electron-Hole Damping. *J. Chem. Phys.* **2004**, *121* (3), 1553–1556. https://doi.org/10.1063/1.1763135.

(94) Priebe, A.; Sinther, M.; Fahsold, G.; Pucci, A. The Correlation between Film Thickness and Adsorbate Line Shape in Surface Enhanced Infrared Absorption. *J. Chem. Phys.* **2003**, *119* (9), 4887–4890. https://doi.org/10.1063/1.1597232.

(95) Wang, H.-C.; Sun, S.-G.; Yan, J.-W.; Yang, H.-Z.; Zhou, Z.-Y. In Situ STM Studies of Electrochemical Growth of Nanostructured Ni Films and Their Anomalous IR Properties. *J. Phys. Chem. B* **2005**, *109* (10), 4309–4316. https://doi.org/10.1021/jp046313o.

(96) Starke, T. K. H.; Johnston, C.; Hill, S.; Dobson, P.; Grant, P. S. The Effect of Inhomogeneities in Particle Distribution on the Dielectric Properties of Composite Films. *J. Phys. Appl. Phys.* **2006**, *39* (7), 1305. https://doi.org/10.1088/0022-3727/39/7/S04.

(97) Moradzaman, M.; Mul, G. Infrared Analysis of Interfacial Phenomena during Electrochemical Reduction of CO2 over Polycrystalline Copper Electrodes. *ACS Catal.* **2020**, *10* (15), 8049–8057. https://doi.org/10.1021/acscatal.0c02130.

(98) Zhang, Z.-M.; Wang, T.; Cai, Y.-C.; Li, X.-Y.; Ye, J.-Y.; Zhou, Y.; Tian, N.; Zhou, Z.-Y.; Sun, S.-G. Probing Electrolyte Effects on Cation-Enhanced CO2 Reduction on Copper in Acidic Media. *Nat. Catal.* **2024**, *7* (7), 807–817. https://doi.org/10.1038/s41929-024-01179-4.

(99) Pilling, M. J.; Le Vent, S.; Gardner, P.; Awaluddin, A.; Wincott, P. L.; Pemble, M. E.; Surman, M. Anomalous Inverse Absorption Features in the Far-Infrared RAIRS Spectra of SnCl4 on Thin-Film SnO2 Surfaces. *J. Chem. Phys.* **2002**, *117* (14), 6780–6788. https://doi.org/10.1063/1.1506142.

(100) Ondry, J. C.; Zhou, Z.; Lin, K.; Gupta, A.; Chang, J. H.; Wu, H.; Jeong, A.; Hammel, B. F.; Wang, D.; Fry, H. C.; Yazdi, S.; Dukovic, G.; Schaller, R. D.; Rabani, E.; Talapin, D. V. Reductive Pathways in Molten Inorganic Salts Enable Colloidal

Synthesis of III-V Semiconductor Nanocrystals. *Science* **2024**, *386* (6720), 401–407. https://doi.org/10.1126/science.ado7088.

(101) Gebre, S. T.; Martinez-Gomez, L.; Miller, C. J.; Kubiak, C. P.; Ribeiro, R. F.; Lian, T. Fano Resonance in CO2 Reduction Catalyst Functionalized Quantum Dots. *J. Am. Chem. Soc.* **2025**, *147* (13), 10966–10973. https://doi.org/10.1021/jacs.4c14499.

(102) Yang, W.; Liu, Y.; Edvinsson, T.; Castner, A.; Wang, S.; He, S.; Ott, S.; Hammarström, L.; Lian, T. Photoinduced Fano Resonances between Quantum Confined Nanocrystals and Adsorbed Molecular Catalysts. *Nano Lett.* **2021**, *21* (13), 5813–5818. https://doi.org/10.1021/acs.nanolett.1c01739.

(103) Gunathunge, C. M.; Li, J.; Li, X.; Hong, J. J.; Waegele, M. M. Revealing the Predominant Surface Facets of Rough Cu Electrodes under Electrochemical Conditions. *ACS Catal.* **2020**, *10* (12), 6908–6923. https://doi.org/10.1021/acscatal.9b05532.

(104) Roiaz, M.; Falivene, L.; Rameshan, C.; Cavallo, L.; Kozlov, S. M.; Rupprechter, G. Roughening of Copper (100) at Elevated CO Pressure: Cu Adatom and Cluster Formation Enable CO Dissociation. *J. Phys. Chem. C* **2019**, *123* (13), 8112–8121. https://doi.org/10.1021/acs.jpcc.8b07668.

(105) Zhang, D.; Virchenko, V.; Jansen, C.; Bakker, J. M.; Meyer, J.; Kleyn, A. W.; Groot, I. M. N.; Berg, O. T.; Juurlink, L. B. F. Characterization of CO Adsorbed to Clean and Partially Oxidized Cu(211) and Cu(111). *J. Phys. Chem. C* **2023**, *127* (50), 24158–24167. https://doi.org/10.1021/acs.jpcc.3c05954.

(106) Zhang, D.; Virchenko, V.; Jansen, C.; Groot, I. M. N.; Juurlink, L. B. F. Adsorption Sites in the High-Coverage Limit of CO on Cu(111). *J. Phys. Chem. C* **2025**, *129* (7), 3493–3497. https://doi.org/10.1021/acs.jpcc.4c07044.

(107) Gunathunge, C. M.; Li, J.; Li, X.; Waegele, M. M. Surface-Adsorbed CO as an Infrared Probe of Electrocatalytic Interfaces. *ACS Catal.* **2020**, *10* (20), 11700–11711. https://doi.org/10.1021/acscatal.0c03316.

(108) Matthews, J. E.; Avilés Acosta, J. E.; Lee, S.-W.; Oh, D.; Lin, T. Y.; Yap, K. M. K.; Chen, J.; Jang, J.-W.; Lee, D. U.; Nielander, A. C.; Jaramillo, T. F. Operando Surface-Enhanced Infrared Spectroscopy Connects Interfacial Dynamics with Reaction Kinetics During Electrochemical CO2 Reduction on Copper. *ACS Catal.* **2025**, *15* (1), 381–391. https://doi.org/10.1021/acscatal.4c05532.

(109) Monai, M. A New Look at Catalyst Surfaces at Work: Introducing Mixed Isotope Operando Infrared Spectroscopy (MIOIRS). *ACS Catal.* **2025**, *15* (2), 1363–1386. https://doi.org/10.1021/acscatal.4c06308.

(110) Ortega, A.; Huffman, F. M.; Bradshaw, A. M. The Adsorption of CO on Pd(100) Studied by IR Reflection Absorption Spectroscopy. *Surf. Sci.* **1982**, *119* (1), 79–94. https://doi.org/10.1016/0039-6028(82)90189-3.

(111) Hollins, P. The Influence of Surface Defects on the Infrared Spectra of Adsorbed Species. *Surf. Sci. Rep.* **1992**, *16* (2), 51–94. https://doi.org/10.1016/0167-5729(92)90008-Y.

(112) Iijima, G.; Inomata, T.; Yamaguchi, H.; Ito, M.; Masuda, H. Role of a Hydroxide Layer on Cu Electrodes in Electrochemical CO2 Reduction. *ACS Catal.* **2019**, *9* (7), 6305–6319. https://doi.org/10.1021/acscatal.9b00896.

(113) Lin, S.; Fishler, Y.; Kwon, S.; Böhme, A. E.; Nie, W.; Richter, M. H.; Yang, M. Y.; Matthews, J. E.; Iton, Z. W. B.; Lee, B. C.; Jaramillo, T. F.; Atwater, H. A.; Goddard, W. A.; Smith, W. A.; See, K. A. Cooperative Effects Associated with High Electrolyte Concentrations in Driving the Conversion of CO2 to C2H4 on Copper. *Chem Catal.* **2025**, *5* (6), 101338. https://doi.org/10.1016/j.checat.2025.101338.

(114) Zhang, L.; Yang, X.; Yuan, Q.; Wei, Z.; Ding, J.; Chu, T.; Rong, C.; Zhang, Q.; Ye, Z.; Xuan, F.-Z.; Zhai, Y.; Zhang, B.; Yang, X. Elucidating the Structure-Stability Relationship of Cu Single-Atom Catalysts Using Operando Surface-Enhanced Infrared Absorption Spectroscopy. *Nat. Commun.* **2023**, *14* (1), 8311. https://doi.org/10.1038/s41467-023-44078-1.

(115) Resasco, J.; Chen, L. D.; Clark, E.; Tsai, C.; Hahn, C.; Jaramillo, T. F.; Chan, K.; Bell, A. T. Promoter Effects of Alkali Metal Cations on the Electrochemical Reduction of Carbon Dioxide. *J. Am. Chem. Soc.* **2017**, *139* (32), 11277–11287. https://doi.org/10.1021/jacs.7b06765.

(116) Resasco, J. A Universal Model of Cation Effects in Electrocatalysis. *JACS Au* **2025**, *5* (11), 5253–5266. https://doi.org/10.1021/jacsau.5c01115.

(117) Gunathunge, C. M.; Ovalle, V. J.; Waegele, M. M. Probing Promoting Effects of Alkali Cations on the Reduction of CO at the Aqueous Electrolyte/Copper Interface. *Phys. Chem. Chem. Phys.* **2017**, *19* (44), 30166–30172. https://doi.org/10.1039/C7CP06087D.

(118) Niu, Y.; Tao, H.; Liu, H.; Li, J.; Lian, C. Cation Regulates Adsorption–Desorption Behaviors To Promote Electrochemical CO2 Reduction Reaction. *ACS Catal.* **2026**, *16* (4), 3903–3913. https://doi.org/10.1021/acscatal.5c08798.

(119) Yuan, X.; Chen, S.; Cheng, D.; Li, L.; Zhu, W.; Zhong, D.; Zhao, Z.-J.; Li, J.; Wang, T.; Gong, J. Controllable Cu0-Cu+ Sites for Electrocatalytic Reduction of Carbon Dioxide. *Angew. Chem.* **2021**, *133* (28), 15472–15475. https://doi.org/10.1002/ange.202105118.

(120) Gunathunge, C. M.; Li, J.; Li, X.; Hong, J. J.; Waegele, M. M. Revealing the Predominant Surface Facets of Rough Cu Electrodes under Electrochemical Conditions. *ACS Catal.* **2020**, *10* (12), 6908–6923. https://doi.org/10.1021/acscatal.9b05532.

(121) Sun, X.; Wu, D.; Wang, J.; Patel, S. B.; Zhu, W.; Yang, J.; Yang, T. T.; Ye, S.; Chen, X.; Zhu, Y.; Qiao, L.; Li, M.; House, S. D.; Su, J.; Saidi, W. A.; Boscoboinik, J. A.; Yang, J. C.; Sharma, R.; Zhou, G. Oscillatory Redox Behavior in Oxides: Cyclic Surface Reconstruction and Reactivity Modulation via the Mars–van Krevelen Mechanism. *Proc. Natl. Acad. Sci.* **2025**, *122* (24), e2422711122. https://doi.org/10.1073/pnas.2422711122.

(122) Yang, J.; Falling, L. J.; Yan, S.; Zhang, B.; Verma, P.; Daemen, L.; Cheng, Y.; Zhao, X.; Zhang, S.; Chen, J.-L.; Yao, B.; Tan, S.; Chae, S.; He, Q.; Nemsak, S.; Wu, Z.; Prendergast, D.; Guo, Y.; Liu, J.; Salmeron, M.; Su, J. Formation of Hydrided Pt-Ce-H Sites in Efficient, Selective Oxidation Catalysts. *Science* **2025**, *388* (6746), 514–519. https://doi.org/10.1126/science.adv0735.

(123) Wang, H.; Shimogawa, R.; Zhang, L.; Ma, L.; Ehrlich, S. N.; Marinkovic, N.; Li, Y.; Frenkel, A. I. Migration and Aggregation of Pt Atoms on Metal Oxide-Supported Ceria Nanodomes Control Reverse Water Gas Shift Reaction Activity. *Commun. Chem.* **2023**, *6* (1), 264. https://doi.org/10.1038/s42004-023-01064-4.

(124) Ding, K.; Gulec, A.; Johnson, A. M.; Schweitzer, N. M.; Stucky, G. D.; Marks, L. D.; Stair, P. C. Identification of Active Sites in CO Oxidation and Water-Gas Shift over Supported Pt Catalysts. *Science* **2015**, *350* (6257), 189–192. https://doi.org/10.1126/science.aac6368.

(125) Green, I. X.; Tang, W.; Neurock, M.; Yates, J. T. Spectroscopic Observation of Dual Catalytic Sites During Oxidation of CO on a Au/TiO2 Catalyst. *Science* **2011**, *333* (6043), 736–739. https://doi.org/10.1126/science.1207272.

(126) Cao, S.; Zhao, Y.; Lee, S.; Yang, S.; Liu, J.; Giannakakis, G.; Li, M.; Ouyang, M.; Wang, D.; Sykes, E. C. H.; Flytzani-Stephanopoulos, M. High-Loading Single Pt Atom Sites [Pt-O(OH)x] Catalyze the CO PROX Reaction with High Activity and Selectivity at Mild Conditions. *Sci. Adv.* **2020**, *6* (25), eaba3809. https://doi.org/10.1126/sciadv.aba3809.

(127) Wietfeldt, H.; Meana-Pañeda, R.; Machello, C.; Reboul, C. F.; Van, C. T. S.; Kim, S.; Heo, J.; Kim, B. H.; Kang, S.; Ercius, P.; Park, J.; Elmlund, H. Small, Solubilized Platinum Nanocrystals Consist of an Ordered Core Surrounded by Mobile Surface Atoms. *Commun. Chem.* **2024**, *7* (1), 4. https://doi.org/10.1038/s42004-023-01087-x.

(128) Tian, Z.; Wang, L.; Deng, Y.; Sun, L.; Zhou, S.; Qian, Z.; Zhao, X.; Zhang, X.; Yang, Y.; Wei, M. Surface Coordination Engineered Single-Atom Catalysts toward Biomass Tandem Conversion. *ACS Catal.* **2026**, *16* (6), 5520–5531. https://doi.org/10.1021/acscatal.5c07118.

(129) Green, I. X.; Tang, W.; Neurock, M.; Yates, J. T. Spectroscopic Observation of Dual Catalytic Sites During Oxidation of CO on a Au/TiO2 Catalyst. *Science* **2011**, *333* (6043), 736–739. https://doi.org/10.1126/science.1207272.

(130) Schouten, K. J. P.; Qin, Z.; Pérez Gallent, E.; Koper, M. T. M. Two Pathways for the Formation of Ethylene in CO Reduction on Single-Crystal Copper Electrodes. *J. Am. Chem. Soc.* **2012**, *134* (24), 9864–9867. https://doi.org/10.1021/ja302668n.

(131) Katayama, Y.; Nattino, F.; Giordano, L.; Hwang, J.; Rao, R. R.; Andreussi, O.; Marzari, N.; Shao-Horn, Y. An In Situ Surface-Enhanced Infrared Absorption Spectroscopy Study of Electrochemical CO2 Reduction: Selectivity

Dependence on Surface C-Bound and O-Bound Reaction Intermediates. *J. Phys. Chem. C* **2019**, *123* (10), 5951–5963. https://doi.org/10.1021/acs.jpcc.8b09598.

(132) Cai, Y.; Yang, R.; Fu, J.; Li, Z.; Xie, L.; Li, K.; Chang, Y.-C.; Ding, S.; Lyu, Z.; Zhang, J.-R.; Zhu, J.-J.; Lin, Y.; Zhu, W. Self-Pressurizing Nanoscale Capsule Catalysts for CO2 Electroreduction to Acetate or Propanol. *Nat. Synth.* **2024**, *3* (7), 891–902. https://doi.org/10.1038/s44160-024-00552-2.

(133) Zhan, C.; Dattila, F.; Rettenmaier, C.; Herzog, A.; Herran, M.; Wagner, T.; Scholten, F.; Bergmann, A.; López, N.; Roldan Cuenya, B. Key Intermediates and Cu Active Sites for CO2 Electroreduction to Ethylene and Ethanol. *Nat. Energy* **2024**, *9* (12), 1485–1496. https://doi.org/10.1038/s41560-024-01633-4.

(134) Chen, C.; Yu, S.; Yang, Y.; Louisia, S.; Roh, I.; Jin, J.; Chen, S.; Chen, P.-C.; Shan, Y.; Yang, P. Exploration of the Bio-Analogous Asymmetric C–C Coupling Mechanism in Tandem CO2 Electroreduction. *Nat. Catal.* **2022**, *5* (10), 878–887. https://doi.org/10.1038/s41929-022-00844-w.

(135) Li, J.; Li, C.; Hou, J.; Gao, W.; Chang, X.; Lu, Q.; Xu, B. Intercepting Elusive Intermediates in Cu-Mediated CO Electrochemical Reduction with Alkyl Species. *J. Am. Chem. Soc.* **2022**, *144* (44), 20495–20506. https://doi.org/10.1021/jacs.2c09378.

(136) Wang, X.; de Araújo, J. F.; Ju, W.; Bagger, A.; Schmies, H.; Kühl, S.; Rossmeisl, J.; Strasser, P. Mechanistic Reaction Pathways of Enhanced Ethylene Yields during Electroreduction of CO2–CO Co-Feeds on Cu and Cu-Tandem Electrocatalysts. *Nat. Nanotechnol.* **2019**, *14* (11), 1063–1070. https://doi.org/10.1038/s41565-019-0551-6.

(137) Gautam, M.; Nkurunziza, F.; Muchharla, B.; Kumar, B.; Spurgeon, J. M. Understanding Electrochemical CO2 Reduction through Differential Electrochemical Mass Spectrometry. *Anal. Chem.* **2025**, *97* (10), 5372–5392. https://doi.org/10.1021/acs.analchem.4c02976.

(138) Zhong, M.; Tran, K.; Min, Y.; Wang, C.; Wang, Z.; Dinh, C.-T.; De Luna, P.; Yu, Z.; Rasouli, A. S.; Brodersen, P.; Sun, S.; Voznyy, O.; Tan, C.-S.; Askerka, M.; Che, F.; Liu, M.; Seifitokaldani, A.; Pang, Y.; Lo, S.-C.; Ip, A.; Ulissi, Z.; Sargent, E. H. Accelerated Discovery of CO2 Electrocatalysts Using Active Machine Learning. *Nature* **2020**, *581* (7807), 178–183. https://doi.org/10.1038/s41586-020-2242-8.

(139) Reichert, A. M.; Piqué, O.; Parada, W. A.; Katsounaros, I.; Calle-Vallejo, F. Mechanistic Insight into Electrocatalytic Glyoxal Reduction on Copper and Its Relation to CO2 Reduction. *Chem. Sci.* **2022**, *13* (37), 11205–11214. https://doi.org/10.1039/D2SC03527H.

(140) Li, Z.; Wang, P.; Lyu, X.; Kondapalli, V. K. R.; Xiang, S.; Jimenez, J. D.; Ma, L.; Ito, T.; Zhang, T.; Raj, J.; Fang, Y.; Bai, Y.; Li, J.; Serov, A.; Shanov, V.; Frenkel, A. I.; Senanayake, S. D.; Yang, S.; Senftle, T. P.; Wu, J. Directing CO2 Electroreduction Pathways for Selective C2 Product Formation Using Single-Site Doped Copper Catalysts. *Nat. Chem. Eng.* **2024**, *1* (2), 159–169. https://doi.org/10.1038/s44286-023-00018-w.

(141) Huang, L.; Gao, G.; Zhao, J.; Roberts, W. L.; Lu, X. Electrocatalytic Upcycling of High-Pressure Captured CO2 to Ethylene. *Nat. Catal.* **2025**, *8* (9), 968–976. https://doi.org/10.1038/s41929-025-01411-9.

(142) Kok, J.; Albertini, P. P.; Leemans, J.; Buonsanti, R.; Burdyny, T. Overcoming Copper Stability Challenges in CO2 Electrolysis. *Nat. Rev. Mater.* **2025**, *10* (7), 550–563. https://doi.org/10.1038/s41578-025-00815-0.

(143) Brandão, L.; Reece, C. Non-Steady State Validation of Kinetic Models for Ethylene Epoxidation over Silver Catalysts. *Catal. Sci. Technol.* **2024**, *14* (13), 3596–3608. https://doi.org/10.1039/D4CY00052H.

(144) Zeng, J. S.; Padia, V.; Chen, G. Y.; Maalouf, J. H.; Limaye, A. M.; Liu, A. H.; Yusov, M. A.; Hunter, I. W.; Manthiram, K. Nonidealities in CO2 Electroreduction Mechanisms Revealed by Automation-Assisted Kinetic Analysis. *ACS Cent. Sci.* **2024**, *10* (7), 1348–1356. https://doi.org/10.1021/acscentsci.3c01295.

(145) Al-Mualem, Z. A.; Lorenz-Ochoa, K. A.; Pan, L.; Ren, H.; Baiz, C. R. Controlling Interfacial Hydrogen Bonding at a Gold Surface: The Effect of Organic Cosolvents. *J. Phys. Chem. Lett.* **2024**, *15* (16), 4391–4399. https://doi.org/10.1021/acs.jpclett.4c00645.

(146) Kastlunger, G.; Wang, L.; Govindarajan, N.; Heenen, H. H.; Ringe, S.; Jaramillo, T.; Hahn, C.; Chan, K. Using pH Dependence to Understand Mechanisms in Electrochemical CO Reduction. *ACS Catal.* **2022**, *12* (8), 4344–4357. https://doi.org/10.1021/acscatal.1c05520.

(147) Xu, A.; Govindarajan, N.; Kastlunger, G.; Vijay, S.; Chan, K. Theories for Electrolyte Effects in CO2 Electroreduction. *Acc. Chem. Res.* **2022**, *55* (4), 495–503. https://doi.org/10.1021/acs.accounts.1c00679.

Acknowledgments

This work was supported by the Director, Office of Science, Office of Basic Energy Sciences, Chemical Sciences, Geosciences and Biosciences Division of the U.S. Department of Energy under Contract DE-AC02- 05CH11231, FWP CH030201 (Catalysis Research Program). M.V.F.G, Y.S, and J.F acknowledge support from the Kavli ENSI Graduate Student Fellowship. M.V.F.G. thanks Dr. Valentin Briega Martos and Prof. Yao Yang for providing ultra-pure D_2O for isotopic substitution experiments. In addition, M.V.F.G. thanks Dr. Marc Figueras-Valls for useful discussions regarding CO coverage on Cu surfaces modeled by density functional theory. We kindly appreciate Dr. Helen Zeng and Prof. Joel Ager for access to and assistance with SEIRAS instrumentation. We also thank Clint Jessel and the College of Chemistry machine shop for their support in fabricating *in situ* cells. Work at the Molecular Foundry was supported by the Office of Science, Office of Basic Energy Sciences, of the U.S. Department of Energy under Contract No. DE-AC02-05CH11231, under proposal number MFP-10283. M.V.F.G. acknowledges Meredith Goudreau for training at the Molecular Foundry. M.V.F.G., N.L, and G.H. acknowledge the Kavli Foundation for supporting this work through the Kavli Berkeley Discovery Fellowship and Berkeley Discovery Hubs program.

Supporting Information

The Supporting Information is available free of charge at XXXXX. Experimental details regarding preparation of electrodes, spectroscopic measurements, tabulated spectral fittings, mode assignments, and control experiments. Figures S1-S35, Table S1-S7, and SI Discussions I-IV (PDF).

ORCIDs

Maria V. Fonseca Guzman (0000-0001-8931-1224)

Yu Shan (0000-0002-8165-8407)

Tianle Wang (0009-0003-3415-354X)

Julian Feijoo (0000-0001-8130-4978)

Nathan Liu (0009-0009-8435-5506)

Jihoon Choi (0000-0002-7311-3087)

Gabrielle Heuer

Andrew Liu (0000-0002-2972-0066)

Prof. Peidong Yang (0000-0003-4799-1684)

Notes

The authors declare no competing financial interest.

Main Text Figures

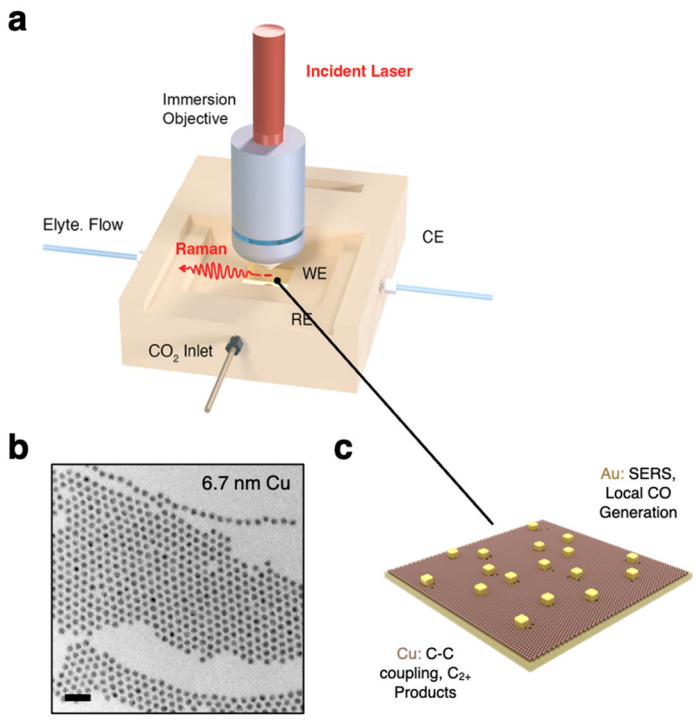

Figure 1. *in situ* electrochemical surface enhanced Raman (SERS) of Cu nanocatalysts. (a) Schematic illustration of electrochemical flow cell used in confocal, SERS configuration. CE, counter electrode; WE, working electrode; RE, reference electrode. (b) TEM image of as-prepared Cu nanocatalysts (Avg. size: 6.7 nm; Scale bar: 20 nm). (c) Schematic illustration of Cu nanocatalysts loaded onto surface enhanced Raman substrates ('WE') and their local electrochemical environment. 45 nm Au nanocubes are used to boost Raman signals and enrich local CO concentration.

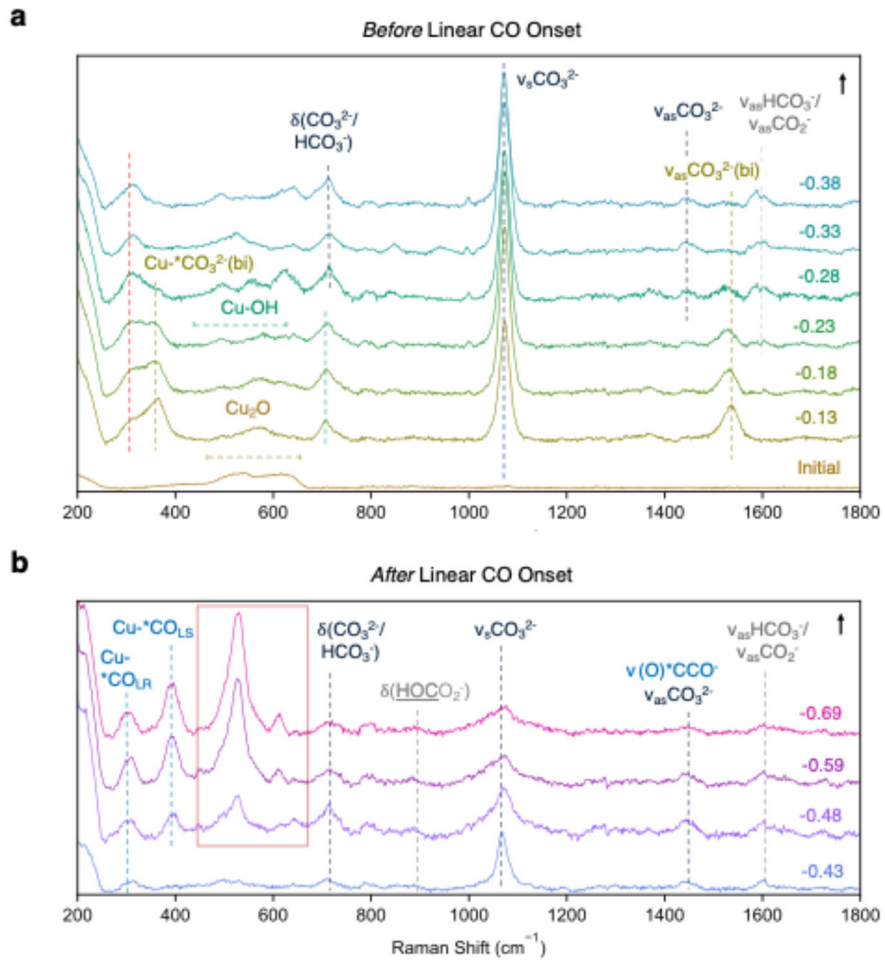

Figure 2. *in situ* SERS spectra of Cu nanocatalysts under stepped electrochemical biases. (a) Spectra evolution before linear CO onset, depicting the reduction and reconstruction stages of Cu nanocatalyst. (b) Spectra collected after linear CO onset, highlighting reaction-induced interactions among surface adsorbates. The modes contributing to the complex band at 435-625 cm^{-1} (red outline) are Cu-*OH (~525 cm^{-1}) and Cu-*O (~603 cm^{-1}) modes. Potentials are applied stepwise and potentiostatically. All measurements are performed in 0.1 M KHCO3 with a 6 mL/ min electrolyte flow and 14 sccm CO2 bubbling rate. Respective peak fitting results is included in **Figure S4**. For full list of assignments for Raman modes, refer to **Table S1**. All spectra are collected using a 633 nm incident laser.

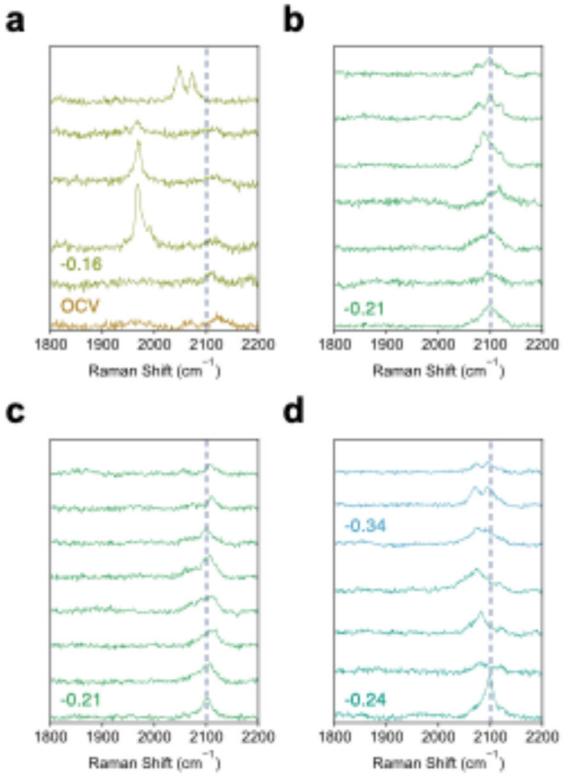

Figure 3. Time-resolved SERS spectra of the CO stretching region collected during the same experiment as Figure 2. Individual traces correspond to sequential measurements acquired approximately **(a)** 1 minute apart, reflecting the temporal evolution of surface intermediates during early catalyst restructuring, or **(b-d)** 3 minutes apart. **(b)** and **(c)** are recorded at the same applied potential but at different times during the experiment, capturing changes in surface state adsorbate population, and SERS fluctuation under otherwise identical electrochemical conditions. Peak fitting for spectra from **(d)** are featured in **Figure S9**.

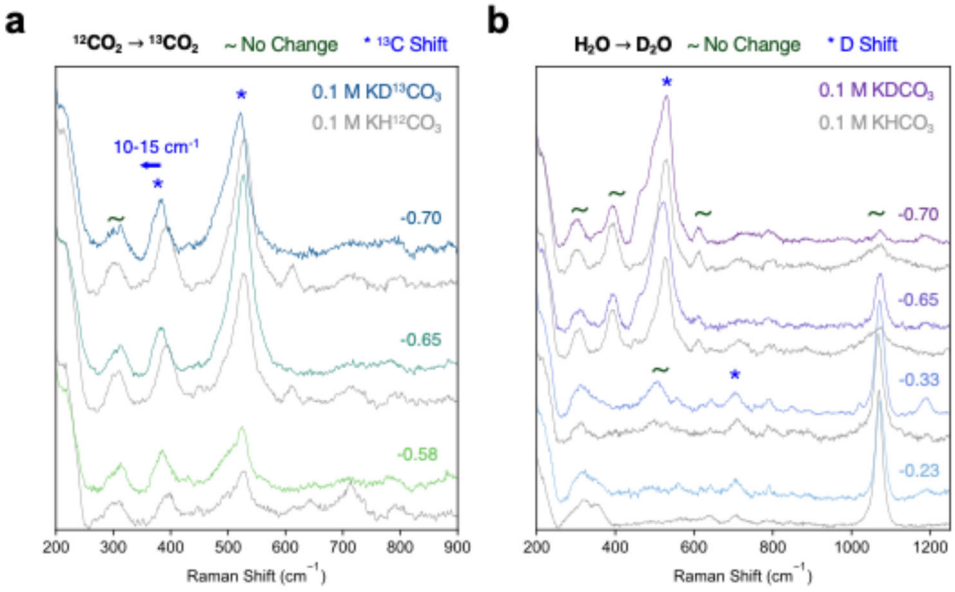

Figure 4. ***in situ*** **SERS spectra of Cu nanocatalysts in isotopically labeled electrolytes.** (a) Spectra collected in 0.1M $KH^{13}CO_3$ (pH = 8.4), showing the expected blue shift of Cu-C mode upon $^{13}CO_2$ substitution (b) Spectra collected in 0.1 M $KDCO_3$ (D_2O, pH = 7.0). Spectra from the standard 0.1 M $KHCO_3$ electrolyte (replotted from **Figure 2b**) are overlaid for comparison. Spectra from the standard 0.1 M $KHCO_3$ electrolyte (replotted from **Figure 1**) are overlaid as grey traces for comparison. All spectra are collected using a 633 nm incident laser. Refer to **Table S1** for a summary of relevant mode assignments.

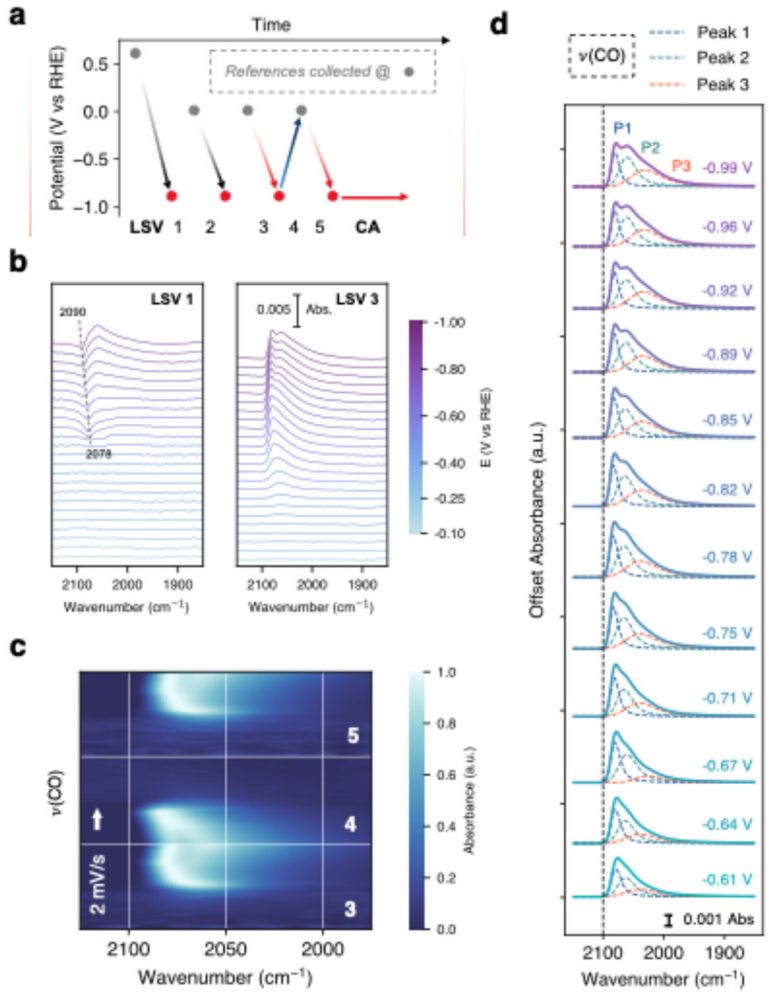

Figure 5. Potential-dependent evolution of the C-O stretch region on Cu nanocatalysts captured by *in situ* SEIRAS. (a) Overview of the SEIRAS experimental workflow. Spectra are acquired during a sequence of linear sweep voltammetry (LSV) scans, where LSV 1, 2, 3, and 5 are cathodic sweeps and LSV 4 is an anodic sweep. Except for LSV 4, which uses the same reference spectrum as LSV 3, each LSV is referenced to a spectrum collected at its respective starting potential (0 V for LSV 2–5 and 0.5 V for LSV 1). (b) Comparison between LSV 1 and LSV 3, where the negative adsorption band near 2080 cm^{-1} in LSV 1 becomes a positive feature in LSV 3. (c) Colormaps with reversibility of emergent twin peaks for CO stretching modes across LSV 3, 4 and 5. Colormap intensities of 1.0 correspond to the CO absorbance maxima of 0.0065 observed during these scans. (d) Peak fitting of CO stretch region during LSV 3 using the sum of skewed Voigts. Additional fits are featured in **Figure S25-S29**.

TOC